Force field optimization by imposing kinetic constraints with path reweighting

P.G. Bolhuis
van 't Hoff Institute for Molecular Sciences, University of Amsterdam, PO Box 94157, 1090 GD Amsterdam, The Netherlands

Z.F. Brotzakis
Department of Chemistry, University of Cambridge, Cambridge CB2 1EW,UK

B.G. Keller
Department of Biology, Chemistry, Pharmacy, Freie Universität Berlin, Arnimallee 22, D-14195 Berlin

(Dated: July 12, 2022)

Empirical force fields employed in molecular dynamics simulations of complex systems can be optimised to reproduce experimentally determined structural and thermodynamic properties. In contrast, experimental knowledge about the rates of interconversion between metastable states in such systems, is hardly ever incorporated in a force field, due to a lack of an efficient approach. Here, we introduce such a framework, based on the relationship between dynamical observables such as rate constants, and the underlying force field parameters, using the statistical mechanics of trajectories. Given a prior ensemble of molecular trajectories produced with imperfect force field parameters, the approach allows the optimal adaption of these parameters, such that the imposed constraint of equal predicted and experimental rate constant is obeyed. To do so, the method combines the continuum path ensemble Maximum Caliber approach with path reweighting methods for stochastic dynamics. When multiple solutions are found, the method selects automatically the combination that corresponds to the smallest perturbation of the entire path ensemble, as required by the Maximum Entropy principle. To show the validity of the approach we illustrate the method on simple test systems undergoing rare event dynamics. Next to simple 2D potentials we explore particle models representing molecular isomerisation reactions as well as protein-ligand unbinding. Besides optimal interaction parameters the methodology gives physical insight into what parts of the model are most sensitive to the kinetics. We discuss the generality and broad implications of the methodology.

arXiv:2207.04558v1 [cond-mat.stat-mech] 10 Jul 2022

I. INTRODUCTION

Often encountered in molecular biology, chemistry, material science and soft condensed matter physics, complex molecular systems can be, in principle, fully characterised by determining their structure, thermodynamics and kinetics. Such characterisation enables understanding these systems' function and how their macroscopic properties arise, and eventually allowing control over their behavior. Experimentally, the first step in characterising (bio)molecular systems is usually to determine the structural and thermodynamic properties [1]. The next step is to identify "kinetic ensembles", which besides the structure and population of the different states also determine their interconversion rates [2–4]. Theoretically, (bio)molecular systems can be modeled by molecular dynamics (MD), which, provided with a faithful underlying interaction potential, yields quantitative structural, thermodynamic, as well as kinetic predictions in microscopic detail [5, 6]. The molecular dynamics community has grown tremendously since the first simulations in the 1950's [5], a trend greatly boosted by the increase in computer power provided by advancements in computer architecture [7, 8], and arguably even more by algorithmic improvements[9], leading to e.g. powerful multiscale models for complex chemical systems. Indeed, molecular dynamics has been shown widely applicable to systems and processes relevant for biology, physics, chemistry and material science[10].

While the above is true in principle, in practice there are two obstacles to obtain kinetic ensembles by MD: First, the interconversion rates are determined by time scales often way beyond what direct MD can access. This is known as the "rare event" problem, or the "sampling" problem [11, 12]. The long time scales are often connected to/caused by high free barriers between states. A vast spectrum of enhanced sampling methods can be applied to overcome such high free energy barriers and address this "sampling problem"[13, 14].

The second potentially more severe and open problem is that the atomistic molecular dynamics force fields are far from perfect, and often face challenges in reproducing the relevant experimental data. While atomistic force fields coarse-grain the quantum mechanical (QM) molecular interactions, thereby making the modelling of many body molecular systems feasible, they suffer from errors associated with the model selection and the usually sparse experimental data sets used for their parametrization [15, 16],e.g. vaporization data for small fragments [15, 17]. Modern approaches also employ Machine Learning to coarse grain the electronic degrees of freedom[18–21]. Current force fields can reach experimental accuracy for such thermodynamic ensemble data [22], but can differ vastly in their kinetic properties [16, 23], because ensemble averages are very sensitive to

the (free) energy differences of the minima in the potential energy function, but not so much to the (free) energies of the barriers. Thus, by parametrizing against thermodynamic ensemble averages one is unlikely to obtain a kinetically accurate force field.

While an accurate bottom-up correction of force field parameters is still challenging for complex molecular systems, one can take a different strategy, namely to correct for force field parametrization inaccuracies in a top-down manner by reweighting atomistic molecular dynamics ensembles using constraints or restraints based on maximum entropy principle in order to match experimental structural and thermodynamic data [24–26]. Taking this strategy further, in previous work we introduced a technique based on the Maximum Caliber approach for continuum path ensembles (CoPE-MaxCal) to incorporate dynamical constraints into unbiased atomistic classical molecular dynamics[4, 27]. The CoPE-MaxCal framework ameliorates the effects of force field parametrization inaccuracies on the kinetic properties of complex molecular systems, by reweighting trajectories based on how far they progress, as measured along a collective variable. Such a strategy was recently further integrated with deep reinforcement learning [28] to enrich molecular simulation ensembles while making it agree with experimental rate constants. While very powerful and generally applicable, the CoPE-MaxCal method does not alter the dynamics of the trajectories in the path ensemble, and therefore is not (directly) suitable for improving the underlying force field parameters.

Systematic and efficient top-down approaches to optimize force field parameters to reproduce thermodynamics and kinetics data are still in their infancy due to sparse solution experiment datasets and lack of efficient, data- or physics-driven optimization algorithms. Even when considering matching just thermodynamics, only a few systematic force field optimisation procedures exist. For instance, recent method developments have enabled parametrizing force fields of large molecules using solution experiment data from NMR, by systematic thermodynamic reweighting methods [29–31]. In addition, artificial intelligence and new open science platforms have entered the field [32, 33]. However, so far, there is no existing systematic strategy to optimize the force field parameters such that an improved force field would match the target (experimental) interconversion rates directly, although procedures for model optimization for dynamical trajectories has been recently proposed[34–36]). Such force fields, capable of representing experimental kinetics, would have a large impact in molecular dynamics, since they would accurately report on transition state structures and populations or processes that are impossible to resolve by experiments [4], thus offering a leverage in, for instance, protein design (e.g by mutations), or regulation (e.g by transition state small molecule binders).

To propose parameters for such a force field, one could perform a naive exhaustive trial and error search, in order to match experimental kinetic data. However, while this sounds straightforward and should work in principle, in practice, this is extremely inefficient as 1) recomputing even a single rate constant is computationally expensive due to the rare event problem and 2) moving randomly in the high dimensional force field parameter space, if at all possible, would take many steps to converge.

In this work we therefore explore an effective way to infer the relationship between force field parameters and kinetic data using only prior ensembles of reference trajectories, and employing techniques to reweight these trajectories. Recently, Donati, Kieninger and Keller explored such path reweighting techniques, which explicitly compute the change in the path action based on a force field perturbation[37–39]. Here, we combine this path reweighting technique with the CoPE-MaxCal approach in order to impose the dynamical constraint, and at the same time select the best solution among multiple solutions: multiple sets of parameters that all give the correct kinetics. This selection thus corresponds to a minimal perturbation, i.e. the change in the force field cause the smallest possible perturbation to the entire path ensemble, while still obeying the constraint.

The computation of the reference trajectory ensemble and the rate constant can be obtained by direct MD, but as mentioned above this is not very efficient. Therefore we employ path sampling methodology, in particular TPS [40, 41] and its descendent single replica transition interface sampling (SRTIS) to efficiently obtain path ensembles[42]. We stress than any rare event method that can compute the reference path ensemble (e.g. FFS[43] or weighted ensemble [44]) is suitable to be used with our methods.

The remainder of the paper is organised as follows. In the next section we develop the above sketched approach. In section III we first validate that the path reweighting can predict rate constant changes. We then optimize the parameters for several model systems to illustrate the effectiveness of the methodology. We end by giving an outlook to which challenges in molecular sciences and other fields our method could be applied.

II. THEORY

A. Maximum Caliber and path reweighting

Consider a system consisting of N atoms. $x \in \mathbb{R}^{3N}$ denotes the configurational state of the system, where $\mathbb{R}^{3N}$ is the $3N$-dimensional position space. We assume that the system evolves according to the overdamped Langevin dynamics [45, 46] in a force field $-\nabla V(x)$ and note that our method can be generalized to underdamped Langevin dynamics [39], so that $x \in \mathbb{R}^{6N}$. We simulate the system using the Euler-Maruyama (EM) method [47] to obtain time-discretized trajectories.

A trajectory is defined as an ordered sequence of frames $\mathbf{x} = \{x_0, x_1, ...x_L\}$, where the subscripts denote the time index. Subsequent frames are separated by a time inter-

val Δt, such that the total duration of a path is $\mathcal{T} = L\Delta t$. These paths $\mathbf{x}$ live in a domain $\mathcal{S}$. The probability for a trajectory in this domain $\mathcal{S}$ is defined as

$$\mathcal{P}[\mathbf{x}] = \frac{1}{\mathcal{Z}}\rho(x_0)\prod_{i=1}^{L} p(x_{i-1} \to x_i), \tag{1}$$

where $\rho(x_0)$ denotes the probability density of the initial condition, usually the Boltzmann distribution $\rho(x) \sim \exp(-\beta V(x))$, with $V(x)$ the potential energy of configuration x, $\beta = 1/k_B T$ the reciprocal temperature, T the temperature and k_B Boltzmann's constant. $p(x_i \to x_{i+1})$ is a short-time Markovian probability representing the dynamical evolution, as given by the integration algorithm and thus depends on $V(x)$.(See eq. 13 in Ref. 39 for $p(x_i \to x_{i+1})$ in the EM algorithm). $\mathcal{Z}$ is a normalization constant such that $\mathcal{P}[\mathbf{x}]$ is normalised with respect to integration over the path ensemble $\int_{\mathcal{S}} \mathcal{D}\mathbf{x}\mathcal{P}[\mathbf{x}] = 1$. ($\mathcal{D}\mathbf{x}$ indicates a path integral over all trajectories $\mathbf{x} \in \mathcal{S}$, in the domain $\mathcal{S}$, see the Appendix for a discussion on the definition of $\mathcal{S}$ in relation to path integrals).

The (relative) path entropy, S or caliber, for any path distribution $\mathcal{P}[\mathbf{x}]$ is given by the Kullback-Leibler divergence D_{KL}

$$D_{KL} = -S = \int_{\mathcal{S}} \mathcal{D}\mathbf{x}\mathcal{P}[\mathbf{x}] \ln \frac{\mathcal{P}[\mathbf{x}]}{\mathcal{P}^0[\mathbf{x}]}. \tag{2}$$

Here, $\mathcal{P}^0[\mathbf{x}]$ denotes the probability of trajectory $\mathbf{x}$ in the reference path ensemble. The maximum caliber principle [48] states that the optimal path probability distribution $\mathcal{P}^{MC}[\mathbf{x}]$ follows from maximising the caliber while satisfying an external constraint s^{exp}.

$$\mathcal{P}^{MC}[\mathbf{x}] = \underset{\mathcal{P}[\mathbf{x}]}{\text{argmax}}\, S[\mathcal{P}||\mathcal{P}^0] \tag{3}$$
$$\text{subject to: } \begin{cases} \int_{\mathcal{S}} \mathcal{D}\mathbf{x}\mathcal{P}[\mathbf{x}] s[\mathbf{x}] = \langle s[\mathbf{x}]\rangle = s^{\text{exp}} \\ \int_{\mathcal{S}} \mathcal{D}\mathbf{x}\mathcal{P}[\mathbf{x}] = 1. \end{cases}$$

That is, $\mathcal{P}^{MC}[\mathbf{x}]$ maximizes the path entropy or caliber, while obeying the constraints given by external constraint s^{exp} and keeping the probability normalized. Even though the specification of the domain $\mathcal{S}$ that is associated to the external constraints is important, we will nonetheless drop $\mathcal{S}$ from the following equations to keep the notation manageable.

Solving eq. 3 can be addressed using the method of Lagrange multipliers. The path Lagrange function is

$$\mathcal{L} = D_{KL} - \mu\left(\int \mathcal{D}\mathbf{x}\,\mathcal{P}[\mathbf{x}] s(\mathbf{x}) - s^{\text{exp}}\right) - \nu\left(\int \mathcal{D}\mathbf{x}\,\mathcal{P}[\mathbf{x}] - 1\right), \tag{4}$$

where the second term imposes the experimental constraint, μ and ν stand for Lagrange multipliers, and the final constraint enforces normalisation. $\mathcal{L}$ depends on the potential energy function $V(x)$ via Eq. 1. The task is now to find the stationary points of the Lagrange function, which constitutes setting to zero the derivatives of $\mathcal{L}$ with respect to the adjustable parameters of the potential energy function.

We make the following ansatz: the adjusted potential energy function $\tilde{V}(x;\mathbf{a})$ differs from the current/prior $V(x)$ by a perturbation $U(x;\mathbf{a})$

$$\tilde{V}(x;\mathbf{a}) = V(x) + U(x;\mathbf{a}), \tag{5}$$

where the change from the current to the new potential energy function can be expressed in terms of m parameters $\mathbf{a} = (a_1, a_2 \ldots a_m)$.

The path probability of the new force field $\mathcal{P}[\mathbf{x}]$ and the path probability of the prior force field $\mathcal{P}^0[\mathbf{x}]$ are related by the relative path probability[39] $\frac{\mathcal{P}[\mathbf{x}]}{\mathcal{P}^0[\mathbf{x}]} = \frac{\mathcal{Z}^0}{\mathcal{Z}(\mathbf{a})} W(\mathbf{x};\mathbf{a})$, thus

$$\begin{aligned}\mathcal{P}[\mathbf{x}] &= \frac{\mathcal{Z}^0}{\mathcal{Z}(\mathbf{a})} W[\mathbf{x};\mathbf{a}]\mathcal{P}^0[\mathbf{x}] \\ &= \frac{\mathcal{Z}^0}{\mathcal{Z}(\mathbf{a})} g(x_0,\mathbf{a}) M[\mathbf{x};\mathbf{a}]\mathcal{P}^0[\mathbf{x}]\end{aligned} \tag{6}$$

where the second equation defines $W[\mathbf{x};\mathbf{a}]$, with

$$g(x_0,\mathbf{a}) = \frac{\exp(-\beta\tilde{V}(x_0;\mathbf{a}))}{\exp(-\beta V(x_0))} = \exp(-\beta U(x_0;\mathbf{a}))$$
$$M[\mathbf{x};\mathbf{a}] = \frac{\prod_{i=0}^{n-1}\tilde{p}(x_{i+1}|x_i,\mathbf{a})}{\prod_{i=0}^{n-1} p_0(x_{i+1}|x_i)}$$

where $p_0(x_{i+1}|x_i)$ is the single-step transition probability of the current (prior) force field, and $\tilde{p}(x_{i+1}|x_i,\mathbf{a})$ is the single-step transition probability of the new force field. $\mathcal{Z}^0/\mathcal{Z}(\mathbf{a})$ is the ratio of the partition function at the current (prior) force field, $\mathcal{Z}^0$, and the partition function at the new (posterior) force field, $\mathcal{Z}(\mathbf{a})$ (see eq. 1). The ratio is linked to the free energy difference of adjusting the force field. We treat $\mathcal{Z}(\mathbf{a})$ as a path probability normalization constant which guarantees that $\int \mathcal{D}\mathbf{x}\mathcal{P}[\mathbf{x}] = 1$. (Note that in previous work e.g. Ref. 41 the $\mathcal{Z}^0$ was set to unity, as the partition function was implicitly embedded in the density $\rho(x_0)$ and the single step transition probabilities were considered normalised. However, in the path reweighting work of Ref. 39 and in this work we cannot assume that anymore, and the partition functions are explicitly taken into account.)

Inserting eq. 6 into eq. 2 yields for the D_{KL}

$$\begin{aligned}D_{KL} &= \frac{\mathcal{Z}^0}{\mathcal{Z}(\mathbf{a})}\int \mathcal{D}\mathbf{x}\mathcal{P}^0[\mathbf{x}]W[\mathbf{x};\mathbf{a}]\ln\frac{\mathcal{Z}^0\mathcal{P}^0[\mathbf{x}]}{\mathcal{Z}(\mathbf{a})\mathcal{P}^0[\mathbf{x}]}W[\mathbf{x};\mathbf{a}] \\ &= \frac{\mathcal{Z}^0}{\mathcal{Z}(\mathbf{a})}\left(\int \mathcal{D}\mathbf{x}\mathcal{P}^0[\mathbf{x}]W[\mathbf{x};\mathbf{a}]\ln W[\mathbf{x};\mathbf{a}] - \ln\frac{\mathcal{Z}(\mathbf{a})}{\mathcal{Z}^0}\right)\end{aligned} \tag{7}$$

where in the second equality we used $\frac{\mathcal{Z}^0}{\mathcal{Z}(\mathbf{a})}\int \mathcal{D}\mathbf{x}\mathcal{P}^0[\mathbf{x}]W[\mathbf{x};\mathbf{a}] = \int \mathcal{D}\mathbf{x}\mathcal{P}[\mathbf{x}] = 1$. This equation can be written as

$$D_{KL} = \frac{\int \mathcal{D}\mathbf{x}\mathcal{P}^0[\mathbf{x}]W[\mathbf{x};\mathbf{a}]\ln W[\mathbf{x};\mathbf{a}]}{\int \mathcal{D}\mathbf{x}\mathcal{P}^0[\mathbf{x}]W[\mathbf{x};\mathbf{a}]} - \ln\int \mathcal{D}\mathbf{x}\mathcal{P}^0[\mathbf{x}]W[\mathbf{x};\mathbf{a}] \tag{8}$$

The total Lagrange function follows then by inserting Eq. 6 into Eq. 4.

$$\mathcal{L} = D_{KL} - \mu \left(\ln \frac{\int \mathcal{D}\mathbf{x}\, W[\mathbf{x};\mathbf{a}]\mathcal{P}^0[\mathbf{x}] \cdot s[\mathbf{x}]}{\int \mathcal{D}\mathbf{x}\, W[\mathbf{x};\mathbf{a}]\mathcal{P}^0[\mathbf{x}]} - \ln s^{\mathrm{exp}} \right) \tag{9}$$

where we now imposed the constraint onto the logarithm of the observable, and the normalisation constraint is automatically obeyed.Therefore we can leave out the third term in the Lagrange function in Eq. 4

Eq. 9 is a central and general result of this work.

Generalizing the Lagrangian in eq. 9 to multiple external constraints ($s_1^{\mathrm{exp}} \dots s_n^{\mathrm{exp}}$) that need to be satisfied simultaneously, yields

$$\mathcal{L} = D_{KL} - \sum_{i=1}^{n} \mu_i \left(\ln \frac{\int \mathcal{D}\mathbf{x}\, W[\mathbf{x};\mathbf{a}]\mathcal{P}^0[\mathbf{x}] \cdot s_i[\mathbf{x}]}{\int \mathcal{D}\mathbf{x}\, W[\mathbf{x};\mathbf{a}]\mathcal{P}^0[\mathbf{x}]} - \ln s_i^{\mathrm{exp}} \right) \tag{10}$$

B. Derivatives of the Lagrange function $\mathcal{L}$

To find the optimal new force field parameters $\mathbf{a}$ for a single constraint, we determine the stationary point of the Lagrange function, i.e. we solve

$$\frac{\partial \mathcal{L}}{\partial a_k} = 0 \qquad \frac{\partial \mathcal{L}}{\partial \mu} = 0 \tag{11}$$

for all $a_1, \dots a_m$, leading to $m+1$ constraint equations.

Obtaining explicit expressions for these constraint equations is easier when defining an auxiliary function $w[\mathbf{x}; a] = \ln W[\mathbf{x}; a]$, so that

$$W[\mathbf{x};\mathbf{a}] = \exp(w[\mathbf{x}; a]) \tag{12}$$

The first term in the Lagrange function, D_{KL} is then

$$D_{KL} = \frac{\int \mathcal{D}\mathbf{x}\mathcal{P}^0[\mathbf{x}] e^{w[\mathbf{x};\mathbf{a}]} w[\mathbf{x};\mathbf{a}]}{\int \mathcal{D}\mathbf{x}\mathcal{P}^0[\mathbf{x}] e^{w[\mathbf{x};\mathbf{a}]}} - \ln \int \mathcal{D}\mathbf{x}\mathcal{P}^0[\mathbf{x}] e^{w[\mathbf{x};\mathbf{a}]} \tag{13}$$

Taking the derivative would give then

$$\frac{\partial D_{KL}}{\partial a_k} = \frac{\int \mathcal{D}\mathbf{x}\mathcal{P}^0[\mathbf{x}] e^{w[\mathbf{x};\mathbf{a}]} w'[\mathbf{x};\mathbf{a}] w[\mathbf{x};\mathbf{a}]}{\int \mathcal{D}\mathbf{x}\mathcal{P}^0[\mathbf{x}] e^{w[\mathbf{x};\mathbf{a}]}} - \frac{\int \mathcal{D}\mathbf{x}\mathcal{P}^0[\mathbf{x}] e^{w[\mathbf{x};\mathbf{a}]} w'[\mathbf{x};\mathbf{a}]}{\int \mathcal{D}\mathbf{x}\mathcal{P}^0[\mathbf{x}] e^{w[\mathbf{x};\mathbf{a}]}} \frac{\int \mathcal{D}\mathbf{x}\mathcal{P}^0[\mathbf{x}] e^{w[\mathbf{x};\mathbf{a}]} w[\mathbf{x};\mathbf{a}]}{\int \mathcal{D}\mathbf{x}\mathcal{P}^0[\mathbf{x}] e^{w[\mathbf{x};\mathbf{a}]}} \tag{14}$$

where the derivative $w'[\mathbf{x};\mathbf{a}] = \partial w[\mathbf{x};\mathbf{a}]/\partial a_k$. Intermediate steps for this derivative are reported in appendix B.

Note that the fractions in Eq.14 can be interpreted as (path) ensemble averages, so that

$$\frac{\partial D_{KL}}{\partial a_k} = \langle w'[\mathbf{x};\mathbf{a}] w[\mathbf{x};\mathbf{a}] \rangle_W - \langle w'[\mathbf{x};\mathbf{a}] \rangle_W \langle w[\mathbf{x};\mathbf{a}] \rangle_W \tag{15}$$

where the bracket subscript W indicates that path ensemble average is calculated with respect to $\mathcal{P}[\mathbf{x}]$, i.e. the reweighted path probability density.

Taking the derivative of the total Lagrange function Eq. 9 with respect to a_k gives

$$\frac{\partial \mathcal{L}}{\partial a_k} = \frac{\partial D_{KL}}{\partial a_k} - \mu \left(\frac{\int \mathcal{D}\mathbf{x}\mathcal{P}^0[\mathbf{x}] e^{w[\mathbf{x};\mathbf{a}]} w'[\mathbf{x};\mathbf{a}] \cdot s[\mathbf{x}]}{\int \mathcal{D}\mathbf{x}\mathcal{P}^0[\mathbf{x}] e^{w[\mathbf{x};\mathbf{a}]} \cdot s[\mathbf{x}]} - \frac{\int \mathcal{D}\mathbf{x}\mathcal{P}^0[\mathbf{x}] e^{w[\mathbf{x};\mathbf{a}]} w'[\mathbf{x};\mathbf{a}]}{\int \mathcal{D}\mathbf{x}\mathcal{P}^0[\mathbf{x}] e^{w[\mathbf{x};\mathbf{a}]}} \right), \tag{16}$$

or again by using path ensemble notation

$$\frac{\partial \mathcal{L}}{\partial a_k} = \frac{\partial D_{KL}}{\partial a_k} - \mu \left(\langle w'[\mathbf{x};\mathbf{a}] \rangle_{Ws} - \langle w'[\mathbf{x};\mathbf{a}] \rangle_W \right), \tag{17}$$

where the Ws subscript now denotes that the path ensemble averages is calculated with respect to the transformed path probability $\mathcal{P}[\mathbf{x}] \cdot s[\mathbf{x}]$. Note that, while the expression $\langle w'[\mathbf{x};\mathbf{a}] \rangle_{Ws}$ can be evaluated for any integrable function $s[\mathbf{x}]$, its interpretation as a path ensemble average is only justified if $s[\mathbf{x}]$ is a positive function.

The entire expression for the derivative is then

$$\frac{\partial \mathcal{L}}{\partial a_k} = \langle w'[\mathbf{x};\mathbf{a}] w[\mathbf{x};\mathbf{a}] \rangle_W - \langle w'[\mathbf{x};\mathbf{a}] \rangle_W \langle w[\mathbf{x};\mathbf{a}] \rangle_W - \mu \left(\langle w'[\mathbf{x};\mathbf{a}] \rangle_{Ws} - \langle w'[\mathbf{x};\mathbf{a}] \rangle_W \right) \tag{18}$$

We can condense this expression even more by dropping the arguments of the functions, which yields

$$\frac{\partial \mathcal{L}}{\partial a_k} = \langle w' w \rangle_W - \langle w' \rangle_W \langle w \rangle_W - \mu \left(\langle w' \rangle_{Ws} - \langle w' \rangle_W \right). \tag{19}$$

The final ingredient for optimisation is the derivative with respect to the Lagrange multiplier μ. This simply is given by the constraint itself

$$\frac{\partial \mathcal{L}}{\partial \mu} = - \left(\ln \frac{\int \mathcal{D}\mathbf{x}\, W[\mathbf{x};\mathbf{a}]\mathcal{P}^0[\mathbf{x}] \cdot s[\mathbf{x}]}{\int \mathcal{D}\mathbf{x}\, W[\mathbf{x};\mathbf{a}]\mathcal{P}^0[\mathbf{x}]} - \ln s_{\mathrm{exp}} \right) \tag{20}$$

or in the condensed form by

$$\frac{\partial \mathcal{L}}{\partial \mu} = - \ln \langle s \rangle_W + \ln s_{\mathrm{exp}} \tag{21}$$

Together, Eqs. 19 and 21, provide the derivatives for finding the stationary point for the Lagrange function, and hence the optimal force field parameters $\mathbf{a}$.

So far, the logarithm of the relative path probability $w(\mathbf{x},\mathbf{a}) = \ln W[\mathbf{x},\mathbf{a}]$ and the path observable $s(\mathbf{x})$ have been abstract functions. Next, section II C derives an expression for the term $\mu \left(\langle w' \rangle_{Ws} - \langle w' \rangle_W \right)$, and section II D derives expressions for w and w' for trajectories generated by the Euler-Maruyama integrator.

C. The rate constant estimate

In the Lagrange function the experimental observable is constrained. While this could be any dynamical observable such a mobility, viscosity, etc., in our work it is taken to be the kinetic observable rate constant. In principle the rate constant can be obtained by counting the number of effective transitions per unit time in a straightforward MD simulation, but this is extremely inefficient due to the rare event problem. Many enhanced sampling methods exist to make rate constant computations more efficient, such as reactive flux approach [49], milestoning [50], forward flux sampling [51], infrequent Metadynamics [52] virtual interface exchange transition path sampling [53] etc [13, 14]. Here, we adopt the framework of transition path sampling [40] and transition interface sampling (TIS)[54], and in particular that of the reweighted path ensemble (RPE) [55]. Defining the metastable stable states A and B using an order parameter or collective variable (CV) λ, with $\lambda_{A,B}$ the boundaries of the states A and B, one can compute the rate constant in the RPE framework from the following expression

$$k_{AB} = \frac{\phi_A \int_A \mathcal{D}\mathbf{x}\mathcal{P}^0[\mathbf{x}]\theta(\lambda_{max}[\mathbf{x}] - \lambda_B)}{\int_A \mathcal{D}\mathbf{x}\mathcal{P}^0[\mathbf{x}]}, \qquad (22)$$

where $\int_A \mathcal{D}\mathbf{x}$ denotes a path integral over paths that leave A and go over the barrier to B, or return to enter A, after which they are terminated. The path length is thus flexible. The frequency with which these paths are sampled is determined by $\mathcal{P}^0[\mathbf{x}]$ and such a (reweighted) path ensemble can be obtained by e.g. TIS. (For a brief discussion on flexible path length ensembles, see appendix A). The $\theta(x)$ is the Heaviside step function and $\lambda_{max}[\mathbf{x}]$ returns the maximum value of the progress order parameter or collective variable (CV) that is able to measure how far the transition has proceeded. Thus, the θ-function in the integral in the numerator selects the paths that reach the boundary of state B, λ_B, i.e., the reactive paths. The fraction is thus equal to the probability of reaching B for paths that leave A. Multiplying with the flux ϕ_A through the first interface λ_0 for paths leaving state A, this indeed gives the rate constant. Using the path reweighting of Eq.6 we obtain

$$k_{AB} = \frac{\phi_A \int \mathcal{D}\mathbf{x}\mathcal{P}^0[\mathbf{x}]W[\mathbf{x};\mathbf{a}]\theta(\lambda_{max}[\mathbf{x}] - \lambda_B)}{\int \mathcal{D}\mathbf{x}\mathcal{P}^0[\mathbf{x}]W[\mathbf{x};\mathbf{a}]}. \qquad (23)$$

Setting $s[\mathbf{x}] = \phi_A\theta(\lambda_{max}[\mathbf{x}] - \lambda_B)$ and the experimental observable to $s^{\exp} = k_{AB}^{\exp}$ in Eq. 9, we obtain the Lagrange function

$$\mathcal{L} = D_{KL} - \mu\Big(\ln \frac{\int \mathcal{D}\mathbf{x}\, W[\mathbf{x};\mathbf{a}]\mathcal{P}^0[\mathbf{x}] \cdot \phi_A\theta(\lambda_{max}[\mathbf{x}] - \lambda_B)}{\int \mathcal{D}\mathbf{x}\, W[\mathbf{x};\mathbf{a}]\mathcal{P}^0[\mathbf{x}]} - \ln k_{AB}^{\exp}\Big), \qquad (24)$$

The derivative of the Lagrangian (eqs. 16 and 17) is

$$\begin{aligned}\frac{\partial\mathcal{L}}{\partial a_k} &= \frac{\partial D_{KL}}{\partial a_k} \\ &- \mu\frac{\phi_A \int \mathcal{D}\mathbf{x}\mathcal{P}^0[\mathbf{x}]e^{w[\mathbf{x};\mathbf{a}]}w'[\mathbf{x};\mathbf{a}]\theta(\lambda_{max}[\mathbf{x}] - \lambda_B)}{\phi_A \int \mathcal{D}\mathbf{x}\mathcal{P}^0[\mathbf{x}]e^{w[\mathbf{x};\mathbf{a}]}\theta(\lambda_{max}[\mathbf{x}] - \lambda_B)} \\ &- \mu\frac{\int \mathcal{D}\mathbf{x}\mathcal{P}^0[\mathbf{x}]e^{w[\mathbf{x};\mathbf{a}]}w'[\mathbf{x};\mathbf{a}]}{\int \mathcal{D}\mathbf{x}\mathcal{P}^0[\mathbf{x}]e^{w[\mathbf{x};\mathbf{a}]}} \\ &= \frac{\partial D_{KL}}{\partial a_k} - \mu\left(\langle w'\rangle_{AB,W} - \langle w'\rangle_{A,W}\right). \qquad (25)\end{aligned}$$

We used the assumption that ϕ_A is not depending on $\mathbf{a}$, and does not depend on $\mathbf{x}$, and thus ϕ_A cancels in the second term. This assumption is justified if the parameters a do not influence the stable state A. In general, of course the parameters can also affect the stable states, and in that case also the change in the flux need to be taken in to account. However, the effect on the flux is expected to be small, in comparison to the change in rate constant due to the barrier height.

In the second equality, the path ensemble average $\langle w'\rangle_{A,W}$ is calculated with respect to the reweighted path probability $\mathcal{P}[\mathbf{x}] = W[\mathbf{x},\mathbf{a}]\mathcal{P}^0[\mathbf{x}]$ (indicated by the subscript W) over all paths that leave A (indicated by the subscript A). The path ensemble average $\langle w'\rangle_{AB,W}$ is calculated with respect to the path probability $\mathcal{P}[\mathbf{x}]\theta(\lambda_{max}[\mathbf{x}] - \lambda_B)$ over all paths that leave A. However, since $\theta(\lambda_{max}[\mathbf{x}] - \lambda_B)$ selects paths that end in B, one can interpret this term as a path ensemble average calculated with respect to the reweighted path probability density $\mathcal{P}[\mathbf{x}]$ (indicated by the subscript W) over all reactive AB trajectories (indicated by the subscript AB) Note the similarities to the temperature derivative of the rate constant in e.g. Ref[56, 57].

The term between brackets in the second equality of Eq. 25 denotes the derivative of the rate constant with respect to the force field parameters.

$$\frac{\partial \ln k_{AB}}{\partial a_k} = \langle w'\rangle_{AB,W} - \langle w'\rangle_{A,W}. \qquad (26)$$

This quantity can thus serve as a first sanity check whether the reweighting approach actually works.

D. Path reweighting using the adapted force field

As defined in Eq. 5, the new force field $\tilde{V}(x)$ differs from the current force field $V(x)$ by a perturbation $U(x;\mathbf{a})$ and the reweighting factor for the stationary density becomes

$$g(x_0,\mathbf{a}) = \frac{\exp(-\beta(V(x_0) + U(x_0,\mathbf{a})))}{\exp(-\beta V(x_0))} = \exp(-\beta U(x_0,\mathbf{a})) \qquad (27)$$

where we left out the normalizing partition function Z, which is included in Ref[39], as it is already included in the path partition normalization constant $\mathcal{Z}(\mathbf{a})$.

Following Ref[39], the path reweighting factor $M[\mathbf{x};\mathbf{a}]$ is

$$M[\mathbf{x};\mathbf{a}] = \exp\left(-\sum_{i=0}^{n-1}\eta_i\cdot\sqrt{\frac{\Delta t}{2k_BT\xi m}}\nabla U(x_i,\mathbf{a})\right) \times \exp\left(-\sum_{i=0}^{n-1}\frac{1}{2}\cdot\frac{\Delta t}{2k_BT\xi m}\left(\nabla U(x_i,\mathbf{a})\right)^2\right) \quad (28)$$

where we use the formulation with the random numbers η[39]. In this definition ξ is the Langevin friction and m the particle mass, as defined in the EM integrator. η_i is the random number used in the ith iteration of the EM integrator out of n time steps (frames) and can be recorded during the simulation a the current force field. Multiplying these two factors gives the total path reweighting $W[\mathbf{x};\mathbf{a}]$. Taking the logarithm yields

$$\begin{aligned}\ln(g(x_0,\mathbf{a})M[\mathbf{x};\mathbf{a}]) = \ln W[\mathbf{x};\mathbf{a}] &= -\beta U(x_0,\mathbf{a}) \\ &- \sum_{i=0}^{n-1}\eta_i\cdot\sqrt{\frac{\Delta t}{2k_BT\xi m}}\nabla U(x_i,\mathbf{a}) \\ &- \sum_{i=0}^{n-1}\frac{1}{2}\cdot\frac{\Delta t}{2k_BT\xi m}\left(\nabla U(x_i,\mathbf{a})\right)^2.\end{aligned} \quad (29)$$

We might further simplify this long expression by defining

$$\kappa \equiv \sqrt{\frac{\Delta t}{2k_BT\xi m}},$$

so that

$$\begin{aligned}w[\mathbf{x};\mathbf{a}] = \ln W[\mathbf{x};\mathbf{a}] &= -\beta U(x_0,\mathbf{a}) \\ &- \sum_{i=0}^{n-1}\eta_i\cdot\kappa\nabla U(x_i,\mathbf{a}) - \sum_{i=0}^{n-1}\frac{1}{2}\cdot\left(\kappa\nabla U(x_i,\mathbf{a})\right)^2,\end{aligned} \quad (30)$$

and the derivative becomes

$$\begin{aligned}\frac{\partial w[\mathbf{x};\mathbf{a}]}{\partial a_k} &= -\beta\frac{\partial U(x_0;\mathbf{a})}{\partial a_k} - \sum_{i=0}^{n-1}\eta_i\cdot\kappa\frac{\partial\nabla U(x_i;\mathbf{a})}{\partial a_k} \\ &- \sum_{i=0}^{n-1}\kappa^2\left(\nabla U(x_i,\mathbf{a})\cdot\frac{\partial\nabla U(x_i;\mathbf{a})}{\partial a_k}\right).\end{aligned} \quad (31)$$

The above equation can be used to compute both the caliber and the derivatives of the Lagrange function. While it is possible to compute the derivative with respect to a_k on the fly, it is even more efficient to be able to compute these a posteriori. This depends on the precise functional form of $U(x,\mathbf{a})$. In case of a linear dependence $\widetilde{V}(x) = V(x) + aU(x)$, the perturbation forces are $a\nabla U(x)$, and the derivate with respect to a is just $\nabla U(x)$. Hence it is convenient to store the sums over $\eta_i\nabla U(x_i,\mathbf{a})$ and $(\nabla U(x_i,\mathbf{a}))^2$ terms for each trajectory explicitly, so that the derivatives can be computed easily for arbitrary values of $\mathbf{a}$. For a non-linear dependence one can still do so, but it becomes more complicated.

III. RESULTS AND DISCUSSION

A. Testing the rate constant derivative

Before embarking on the full problem of force field optimization, we first will check the path reweighting method, by computing the derivative of the rate constant, i.e. Eq. 26.

$$\frac{\partial\ln k_{AB}}{\partial a_k} = \left\langle\frac{\partial w[\mathbf{x};\mathbf{a}]}{\partial a_k}\right\rangle_{AB,W} - \left\langle\frac{\partial w[\mathbf{x};\mathbf{a}]}{\partial a_k}\right\rangle_{A,W} \quad (32)$$

Thus the rate constant derivative is equal to the difference between two path ensembles averages. This is a general expression and can be related to the Arrhenius law, and estimates of the activation energy from path sampling[56, 57].

1. *Diatomic system*

Now we are ready to look at a specific system. We first investigate a simple diatomic system in which the two atoms are held together by a bistable potential (in dimensionless units)

$$\beta V_0(r) = 10((r-2)^2-1)^2 \quad (33)$$

where r is the (dimensionless) distance between the atoms. There are two minima located at $r = 1$ and $r = 3$. We can thus interpret this system as a diatom that has a compact state an extended state, separated by barrier with a height of 10 k_BT. Due to the 2D nature of the system, the expanded state has more entropy, and is expected to be (slightly) more stable. Next, we add a Gaussian to the potential

$$\beta V(r) = 10((r-2)^2-1)^2 + a\exp(-20(r-2)^2) \quad (34)$$

Figure 1 depicts this potential for several values of a, ranging from $a = 0$ to $a = 25$.

We add a perturbation of the same Gaussian form

$$\beta U(r;a) = \Delta a\exp(-20(r-2)^2), \quad (35)$$

so that the perturbed total potential is

$$\beta\tilde{V}(r) = \beta V_0(r) + (a+\Delta a)\exp(-20(r-2)^2) \quad (36)$$

As the perturbation is not affecting the stable states we can neglect the first term in Eq 31,

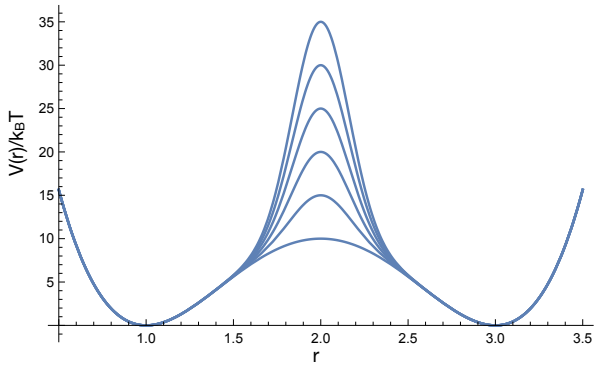


FIG. 1. Total interaction potentials $\beta V(r)$ in the diatomic system for different settings of a. The lowest curve is the bistable potential $\beta V_0(r)$, i.e. $a = 0$. Each curve above corresponds to an increased a in steps of $5k_BT$.

For this test we compute the rate constant derivatives for $\Delta a = 0$, that is, a zero perturbation. In particular, then the gradient of the force in the last term of Eq. 31 vanishes, leaving

$$\left(\frac{\partial w[\mathbf{x};a]}{\partial a}\right)_{\Delta a=0} = -\sum_{i=0}^{n-1} \eta_i \cdot \kappa \frac{\partial \nabla U(x_i,a)}{\partial a_k}. \qquad (37)$$

We can now sample the transition over the barrier in this diatomic system using SRTIS[42]. The stable states are defined as $\lambda_A = 1$ and $\lambda_B = 3$, while the interfaces were put at $\lambda = \{1.30, 1.35, 1.40, 1.45, 1.50, 1.55, 1.60, 1.65, 1.70, 1.72, 1.74, 1.76, 1.78, 1.80, 1.82, 1.84, 1.86, 1.88, 1.90, 1.92, 1.94, 1.96, 1.98\}$. The Langevin settings are $\gamma = 2.5$ and $dt = 0.001$. Integration is via the EM algorithm. Sampling 10000 cycles with SRTIS [42], where each cycle consisted of 100 shots, 100 interface exchanges, and 100 state swaps, resulted in a path ensemble for each interface. The measured crossing histograms were joined with WHAM [58], which together with the effective positive flux through the first interface[13, 42, 54] leads to rate constant estimates over the barrier. The WHAM also allowed to assign a weight to each trajectory in the path ensemble. Each of these trajectories can be evaluated in terms of the path action and its derivatives.

The results are given in Table I. For different values of a the (log) rate constant k is given, as well as the rate derivative, and the flux through the first interface. The rate constant is here without the flux term, so the true rate constant is k times the flux. The rate constant for the forward (expansion of the dimer) and reverse (contraction of the dimer) processes are slightly different, caused by the difference in stability, arising from the larger entropy in the expanded state.

Note that the barrier height scales with the parameter a. In principle, the logarithm of the rate constant therefore should roughly follow $v_{bar} = 10 + a$, in our case. Clearly, this is not strictly obeyed, even when taking the flux into account. This could be due to the used integrator, but more likely because the diffusive barrier crossing is best described by Kramers' theory, which has a dependency on the curvature of the barrier, which is increasing with a. Hence, we expect the rate constant behave as $\ln k = c_0 + c_1 a + c_2 \ln a$ with c_i some fit parameters, which indeed seems to be the case.

We can now also compare the derivative of the rate constant $d\ln k/da$, as computed from the path action averaged over the path ensemble, directly with the numerical derivative of the measured rates. This is shown in figure 2. Clearly the agreement is good, especially considering

TABLE I. Logarithmic rate constant, path action derivative and fluxes for the diatom system. The first set of result are for the forward expansion transition, the second set for the backward contraction transition. Note that the second set shows a systematically lower rate constant because the expanded state is slight more stable due to a higher entropy.

a	ln k	dlnk/da	flux ϕ_A
1	-9.01672	-0.774092	0.002443
2	-9.83885	-0.82772	0.002391
3	-10.716	-0.881064	0.002415
4	-11.5969	-0.895259	0.002351
5	-12.5809	-0.909444	0.002406
10	-17.1724	-0.937627	0.002406
15	-22.231	-0.944568	0.002425
20	-26.728	-0.966014	0.002405
1	-9.89133	-0.777035	0.001879
2	-10.6125	-0.813796	0.001862
3	-11.4701	-0.861863	0.001870
4	-12.3586	-0.891026	0.001825
5	-13.287	-0.912954	0.001892
10	-18.2126	-0.934554	0.001881
15	-22.9438	-0.947677	0.001864
20	-27.7684	-0.955044	0.001874

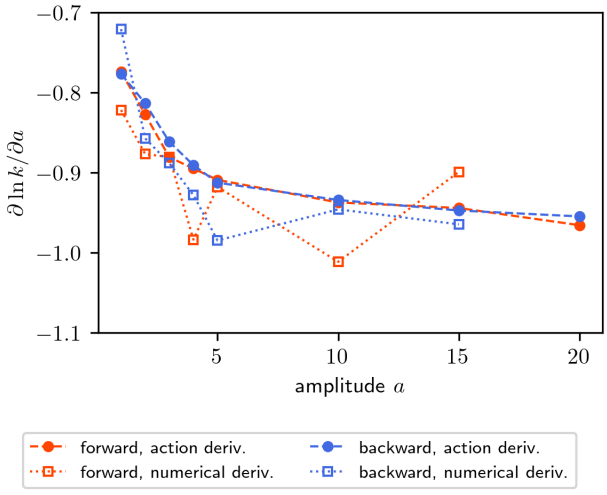


FIG. 2. The derivative of the (log) rate constant with respect to the amplitude a of the Gaussian perturbation for the diatomic system. The path action based derivative is compared to the numerical derivative.

the different origins of the two data sets. In particular the numerical derivative is prone to large errors. Note that the rate constant derivatives for the forward and backward process are (almost) equal, because the stable states are not affected by changing a. Thus, the rate constant is affected in exactly by the same factor by the change in the barrier potential.

2. *Triatomic system*

Next, we consider a 2D triatomic system in which three atoms interacting with WCA potentials [59] are bound by a harmonic potential that has a minimum at a certain equilibrium bond distance: $V(r) = \frac{1}{2}a(r - r_{eq})^2$. This trimer can undergo an isomerisation transition where one particle passes between the other two, hence changing from a clock wise to anticlockwise arrangement of the (labeled) particles (see Fig. 3). Note that this system was also studied in Ref[41]. We look at isomerisation rate constants for this trimer and measure the rate constants and its derivative as function of the force constant a, and the equilibrium distance r_{eq}. In fact, since we are interested in the changes from a reference system we define the perturbed system as

$$\tilde{V}(r) = \frac{1}{2}(a + \Delta a)(r - (r_{eq} + \Delta r_{eq}))^2. \qquad (38)$$

We can again look at the derivatives to the rate constants

$$\left(\frac{\partial \ln k_{AB}}{\partial a}\right)_{\Delta a=0},$$

and

$$\left(\frac{\partial \ln k_{AB}}{\partial r_{eq}}\right)_{\Delta r_{eq}=0}.$$

Also here the path action derivative does not contain the second term in Eq.31, as we set the perturbation $\Delta a = 0$:

$$\left(\frac{\partial w[\mathbf{x}; a]}{\partial a}\right)_{\Delta a=0} = -\sum_{i=0}^{n-1} \eta_i \cdot \kappa \frac{\partial \nabla U(x_i, a)}{\partial a_k}. \qquad (39)$$

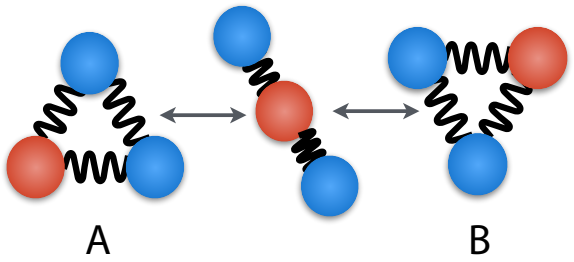


FIG. 3. Cartoon of a 2D triatomic system held together by harmonic springs. The trimer can isomerise as indicated in the figure. For illustrative purposes one particle is colored red. Note that we focus on only one of the 3 possible equivalent transition channels.

We can sample the transition over the barrier in the triatomic system using SRTIS. The collective variable used to defined stable states and interfaces is the shortest distance r_{perp} of the hopping particle to the axis between the two remaining particles. This distance is negative or positive depending on which side the hopping particles is located. the CV is then transformed as

$$\lambda = \frac{3}{2}\left(\frac{r_{perp}}{r_{eq}} + 1\right)$$

The stable state A is defined as $\lambda < \lambda_A = 0$. The stable state B is defined from the other side and is also $\lambda_0 < \lambda_B = 0$. Note that since the reference state is different, both definitions refer to different states, even if the value of λ is equal. Interfaces were defined at $\lambda = 0.4, 0.45, 0.50, 0.55, 0.60, 0.65, 0.70, 0.75, 0.80, 0.85, 0.90, 0.95, 1.00, 1.05, 1.10, 1.15, 1.20, 1.25, 1.30, 1.35, 1.40, 1.45, 1.50, 1.55, 1.60, 1.65, 1.70, 1.75, 1.80$. The Langevin settings are $\gamma = 2.5$ and $dt = 0.001$. Integration is done via the EM algorithm. Sampling was done using the same settings as for the diatom system, leading, after WHAM analysis of the crossing probability histograms to the rate constant estimates over the barrier, as well as to an ensemble of weighted paths, that can be evaluated in terms of the path action and its derivatives.

The derivatives are shown in Figs.4 and 5. The derivative of the (log) rate constant with respect to a is flat, as expected since a is a prefactor to the perturbation. The value of the derivative is very close to the analytical value of -0.375. For the derivative with respect to the equilibrium distance r_{eq} the situation is very different. The rate constant varies in a non-monotonic way.

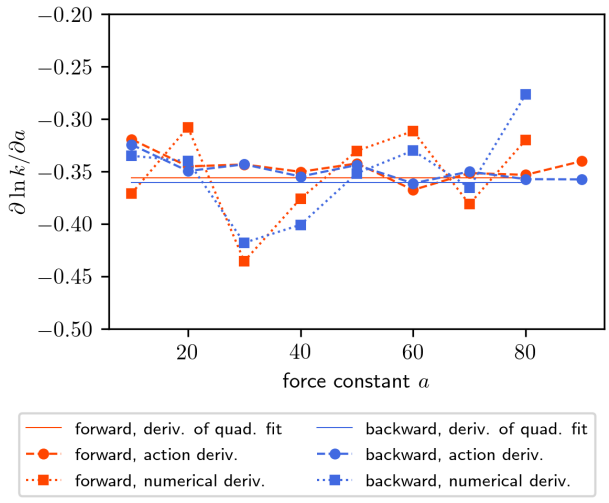


FIG. 4. The derivative of the (log) rate constant with respect to the force constant a of the harmonic potential for the diatomic system. The path action based derivative is compared to the numerical derivative. The derivative of the (linear) fit to the log rate constant is also shown.

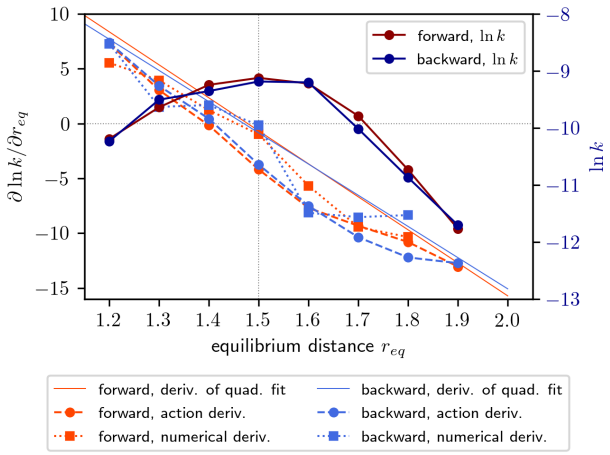


FIG. 5. The derivative of the (log) rate constant with respect to the equilibrium distance r_{eq} of the harmonic potential for the diatomic system. The path action based derivative is compared to the numerical derivative. Also shown is the derivative of the (quadratic) fit to the rate constant. The (log) rate constant is also included, and shows a maximum around $r_{eq} = 1.5$

At shorter distance r_{eq} the particles are forced on top each other and repel each other again, lowering the rate constant again for low values. At larger distance the particles have to travel more before they can overcome the barrier, leading also to higher barriers and lower rates. The maximum rate constant translates as a change of sign in the derivative. The values of the action derivative agree with the rate constant derivatives, although not as good as those for the a parameter, possibly because r_{eq} affects the path ensemble much stronger than a does. Also the non-linearity of the rate dependence on r_{eq} can play a role here.

B. Optimisation of the Lagrange function

Now that the rate constant derivatives are tested, and well-predicted by our path reweighting approach, we can turn to the optimisation of the force field parameters. Here we focus first on the trimer system, since this has two parameters to optimize, which both can be tweaked to reproduce the imposed rate. To optimise the Lagrange function Eq.9, we have to be able to compute the Lagrange function as a function of parameters not only at zero perturbation, but also for the reweighted path ensemble $W[\mathbf{x}; a]$. Moreover, we need to be able to take its derivatives at nonzero perturbation.

To do so, we keep track of several variables for each path that are appearing in the polynomial expansion of the path action. To be precise, we compute the path action as

$$
\begin{aligned}
& w[a, r; \Delta a, \Delta r] = \\
& - \beta(\Delta a\, u_{0,da2} + (a + \Delta a)\Delta r\, u_{0,dadr} + \frac{3}{2}(a + \Delta a)\Delta r^2) \\
& + \Delta a\, \eta f_{da} + (a + \Delta a)\Delta r\, \eta f_{dr} - \Delta a^2 f^2_{da^2} \\
& - 2\Delta a(a + \Delta a)\Delta r\, f^2_{dadr} - \Delta r^2 (a + \Delta a)^2\, f^2_{dr2}, \qquad (40)
\end{aligned}
$$

where the different u and ηf terms refer to the specific contribution to the energy in the first time slice 0 and the random number force (gradients), respectively (see Eq. 31). The f^2 terms refer to the gradient square terms. Using these quantities it is easy to compute the derivatives $dw[a, r; \Delta a, \Delta r]/da$ and $dw[a, r; \Delta a, \Delta r]/dr$. From these we compute the path ensemble averages $\langle w'w' \rangle_W$, $\langle w \rangle_W$ and $\langle w' \rangle_W$. Finally, we construct the reweighted rate constant $\ln k[a, r; \Delta a, \Delta r]$ D_{KL}, and the Langrange function $\mathcal{L}$, from the above equations.

For a particular set of values of $a = 20$ and $r_{eq} = 1.5$ we computed the path ensemble. In figure 6, we show the D_{KL}, and the log rate constant $\ln k[a, r; \Delta a, \Delta r]$ on top of each other as a function of Δa and Δr. As expected, the D_{KL} is minimal for the reference value $\Delta a = 0, \Delta r = 0$, that is, at zero perturbation.

The reweighted rate constant is identical to the predicted rate constant from the prior path ensemble for $\Delta a = 0, \Delta r = 0$, but clearly varies if the system is perturbed. Note that Δa seems to have the strongest effect

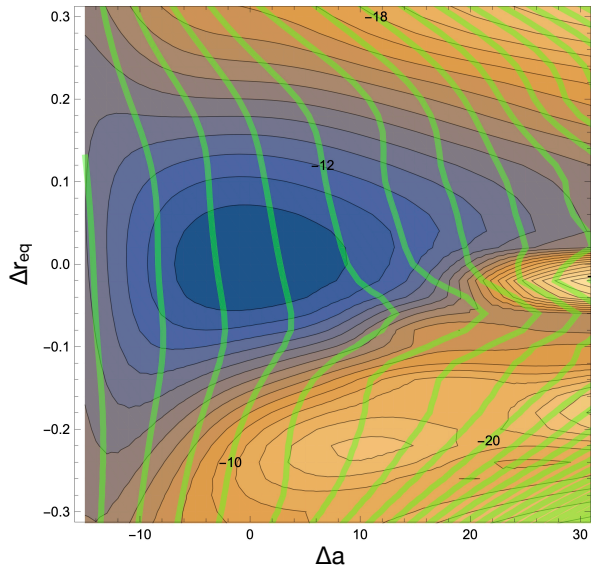


FIG. 6. Contour plot of D_{KL} (shaded contour plot) for the triatomic system as function of $\Delta r, \Delta a$ for a reference path ensemble obtain at $r_{eq} = 1.5, a = 20\ k_B T$. Note that the minimum value of D_{KL} is at the origin, as expected. On top of the shaded contour plot is a green line contours plot of the predicted rate constant $\ln k_{AB}$, for the settings. Several numerical values of the contours are indicated. The graphical solution to optimisation problem is to pick an imposed green contour and minimize the D_{KL} along this contour.

TABLE II. Results of the optimization procedure for different imposed log rates. The first set allows both parameters to vary; the second set varies only Δa, and the third only Δr

$\ln k_{AB}^{exp}$	μ	Δa	Δr	D_{KL}
-8	-0.162561	-3.03452 -	0.00290183	0.0831778
-12	0.27589	8.43988	0.01461	0.454862
-16	0.303009	19.0579	0.0440781	1.68525
-20	0.280855	29.1066	0.0659962	2.87969
-8	-0.164467	-3.06428	0	0.0840814
-12	0.317654	8.84244	0	0.489055
-16	1.00039	19.8675	0	2.98142
-20	0.57278	28.7734	0	6.95817
-12	0.587054	0	0.258986	4.18148
-16	0.286304	0	0.385952	5.617
-20	0.547232	0	0.490967	6.96569

in changing the rate. In contrast, for a similar change in D_{KL} varying Δr also changes the rate constant but not as dramatically. Indeed, the D_{KL} is very sensitive to the Δr, already indicating that it is probably better to adjust a than r_{eq}.

When we change the rate constant from the observed value of $\ln k_{AB} = -9$ to the new value $\ln k^{exp}$ we need to compute the derivatives and optimise the Lagrange function. We apply the method of Ref. [60]. This iterative method starts at certain initial values and slowly converges to the solution. The solution for the most optimal set of $\{\Delta a, \Delta r\}$ is shown in table II. In this table we show several sets of optimal solutions, as a function of imposed k_{AB}^{exp}. The first set shows the optimal solution for both Δa and Δr. The other two sets we optimised for only one of the two parameters, and set the other to zero. From the value of D_{KL} (which is identical to the negative of the Lagrange function $\mathcal{L}$ when the constraints are obeyed) it is clear that this is always less optimal than the two parameter solution, thus illustrating the need for multi-parameter force field optimization. Also note that the further the imposed $\ln k_{AB^{exp}}$ is from -9, the more $\mathcal{L}$, and thus D_{KL} deviates.

C. Dissociation from a LJ cluster, a model for ligand-protein dissociation

Having shown that we can apply our framework to model systems for molecular reaction, we explore in this section a slightly more elaborate system, which also has interesting physical properties, namely particle dissociation from a cluster of LJ particles. Such a process can be viewed as analogous to the ligand unbinding, which is an important problem in biophysics[61, 62]. Moreover, it can be seen as dissociation for small nano-clusters[63–68].

1. *Model*

We describe the dissociation transition using a model of Lennard-Jones (LJ)-like particles. We first consider a 7 particle setup in two dimensions, indicated in Fig. 7. In the simplest instance of this model all particles are kept fixed except the red particle, which can dissociate into the bulk. This red particle interacts with both the central blue particle and the green particles via an attractive LJ-like interaction potentials with adjustable depths. The interaction with the gray particles is purely repulsive and given by a standard repulsive WCA potential [59]. Setting the particle diameter as the unit of length $\sigma = 1$, and denoting the red particle with index 0, the total energy is thus

$$V_{tot} = V_{\epsilon_1}(r_{0c}) + \sum_{j \in green} V_{\epsilon_2}(r_{0j}) + \sum_{j \in gray} V_{wca}(r_{0j}), \tag{41}$$

where the (adjustable) potentials $V_\epsilon(r)$, in units of $k_B T$, are given by

$$\beta V_\epsilon(r) = \begin{cases} 4\epsilon_0(r^{-12} - r^{-6}) + v_\epsilon & r < 2^{1/6} \\ 4\epsilon(r^{-12} - r^{-6} + v_s) & 2^{1/6} < r < r_c \\ 0 & r > r_c \end{cases} \tag{42}$$

Here, the constants v_s and v_ϵ shift the potential such that the potential is zero at the cutoff $r_c = 1.5$, and continuous at the minimum $r = 2^{1/6}$. ϵ is the (reduced/dimensionless) depth of the potential, while $\epsilon_0 = 1$ is the standard reference value for the potential. For this particular cutoff it follows $v_s = r_c^{-6} - r_c^{-12} = 0.0800841$, and $v_\epsilon = (1 - \epsilon) + 4\epsilon v_s$;

The switching at the minimum of the potential is done to avoid problems with the rather steep repulsive part of the potential arising for the high values of ϵ_1 required to bind the particle. Therefore, we chose to keep the repulsive part of the potential equal to the standard WCA potential, i.e. not scale with ϵ. In this way, only when the particles are in the attractive part of the potential they contribute to the path action derivatives, making evaluation of the path action more robust. Note that this does not change the generality of our approach.

In the first model, we keep the all particles fixed except the red dissociating particle, so the only important interactions are that of the red particle with the 6 other particles. In the second model, we allow the other particles to move as well. To keep the cluster together, we apply an additional potential that binds the non-red particles to the central blue particle by an additional strong

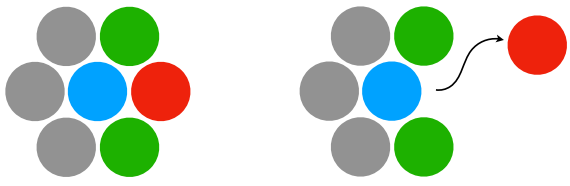


FIG. 7. Cartoon of the 2D dissociation model. The red particle, originally bound to the central (blue) and outer (green) particles, can escape into the bulk.

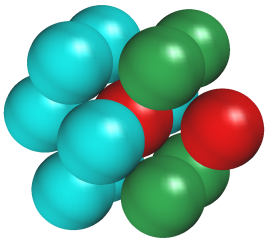


FIG. 8. Cartoon of the 3D dissociation model. The escaping outer red particle is initially bound to the central particle (also red) and 4 outer green particles.

LJ interaction $V_{\epsilon_3}(r)$, with $\epsilon_3 = 20$. While this keeps the cluster intact, rearrangements are still possible. We avoid these by imposing an additional weak harmonic spring between neighbouring particles with a spring constant $k = 1$ (this of course excludes the red particle).

The result is a fluctuating cluster of 6 particles, that can expel the red particle. During the dissociation, the green particles can move closer to each other, gaining in entropy. We can interpret this simple model as representing a ligand unbinding reaction, e.g. of a protein, in which the protein binding pocket slightly rearranges upon (un)binding.

Finally, in order to show that our methodology easily extends to 3D systems, we consider a 3D version of model with 13 LJ particles as depicted in Fig. 8. Here 4 outer green particles bind the ligand with an attraction ϵ_2.

2. *Path ensembles*

We first start exploring the fixed 7-particle model. Setting the central particle interaction to $\epsilon_1 = 10$, and the green particle interaction to $\epsilon_2 = 1$, we sample unbinding transitions using SRTIS. The order parameter λ used is the center-to-center distance between the red and blue particles. Stable states were defined as $r < 2^{1/6}$ and $r > 2.5$ for the initial and final states respectively (Note that beyond $r = 2.5$ the ligand cannot yet be considered escaped to the bulk. While, it is possible to take this into account see e.g. Ref[69, 70], we assume here for simplicity that the ligand is dissociated). Interfaces were positioned at $\lambda = 0.15, 0.15, 0.20, 0.25, 0.30, 0.35, 0.40, 0.50, 0.60, 0.70, 0.80, 1.00$, with respect to the minimum distance $r_A = 2^{1/6}$. We integrate the equations of motion using the EM integrator with a time step of $dt = 0.001$ and a friction of 2.5. In total we perform 10^5 shooting and replica exchange moves. Acceptance ratios for the shooting move ranges from 0.4 for the first interface to 0.15 for the last interface. Replica exchange moves where accepted around 50%. Path lengths vary from 50 timesteps for the first interface to a few thousand for the last interface. The crossing probability of the final interface (obtained from WHAM) is $\ln P(\lambda_B|\lambda_1) = -6.567$. The flux of the first interface is $\phi = 0.003550$ The total rate constant is thus $k_{AB} = 5 \times 10^{-6}$ per in unit of time step. Note that, when optimising the rate constant, we assume that the fluxes are not altered much (as above), and we only have to consider the crossing probability.

We performed also runs for the flexible cluster. The simulation for the flexible 2D cluster is similar to the fixed case, but the results will be very different, as shown below.

We can now use our framework to look for the best set of new parameters $\epsilon_1' = \epsilon_1 + \Delta\epsilon_1$ and $\epsilon_2' = \epsilon_2 + \Delta\epsilon_2$. The path action is given by

$$\begin{aligned} w[\epsilon_1, \epsilon_2, ; \Delta\epsilon_1, \Delta\epsilon_2] &= -\beta(\Delta\epsilon_1\, u_{0,\epsilon_1} + \Delta\epsilon_2\, u_{0,\epsilon_2}) \\ &+ \Delta\epsilon_1\, \eta f_{\Delta\epsilon_1} + \Delta\epsilon_2\, \eta f_{\Delta\epsilon_2} \\ &- \Delta\epsilon_1^2 f^2_{\Delta\epsilon_1^2} - \Delta\epsilon_1\Delta\epsilon_2 f^2_{\Delta\epsilon_1\Delta\epsilon_2} - \Delta\epsilon_2^2 f^2_{\Delta\epsilon_2^2 de 2^2} \end{aligned} \tag{43}$$

where the u_0, ηf-functions and f-functions involve the potential energy of the first slice, and the gradient of the potential energy, c.f. Eq.30 and Eq.40. Note that as mentioned above only the attractive part of the potential has to be taken into account.

3. *Caliber/D_{KL} and rate constant predictions*

Our framework then gives the rate constant predictions for the altered parameters, as well as the caliber or D_{KL}. Fig. 9 presents both predictions as contour plots. The green contours delimit the (log of the) dissociation rate constant (in fact, the crossing probability) predictions, while the blue-ochre contours depict the D_{KL}. Several conclusions follow from this figure. The first is that for the fixed cluster the D_{KL} contours show some anti-correlation in the two parameters. This indicates that the path ensemble is least disturbed when a increase in ϵ_2 is compensated by a decrease of ϵ_1. The D_{KL} contours also are slightly asymmetric, showing a larger sensitivity to negative values of ϵ_2. As this parameter is set to the relatively low value of $\epsilon_2 = 1$, reduction below $\Delta\epsilon_2 < -1$, will therefore reverse the sign of the attractive interaction, which of course completely alters the systems. The flexible cluster Fig. 9B shows no such anti-correlation in D_{KL}, indicating that the compensating effect has largely disappeared.

The second observation is that the green rate constant contours are roughly linear with a negative slope This indicates that both increasing ϵ_1 and ϵ_1 have similar effects for a large variety of values. So, to have a similar decrease in rate constant one could choose either to increase ϵ_1 or ϵ_2. Note that the slope of the contour is roughly -0.5, as there are two outer particles (green) and only 1 central particle, so changing their interaction strengths ϵ_2 has therefore twice the effect. This observation indicates that ϵ_1 and ϵ_2 are more or less interchangeable, and one can choose many combinations for arriving at the same rate constant.

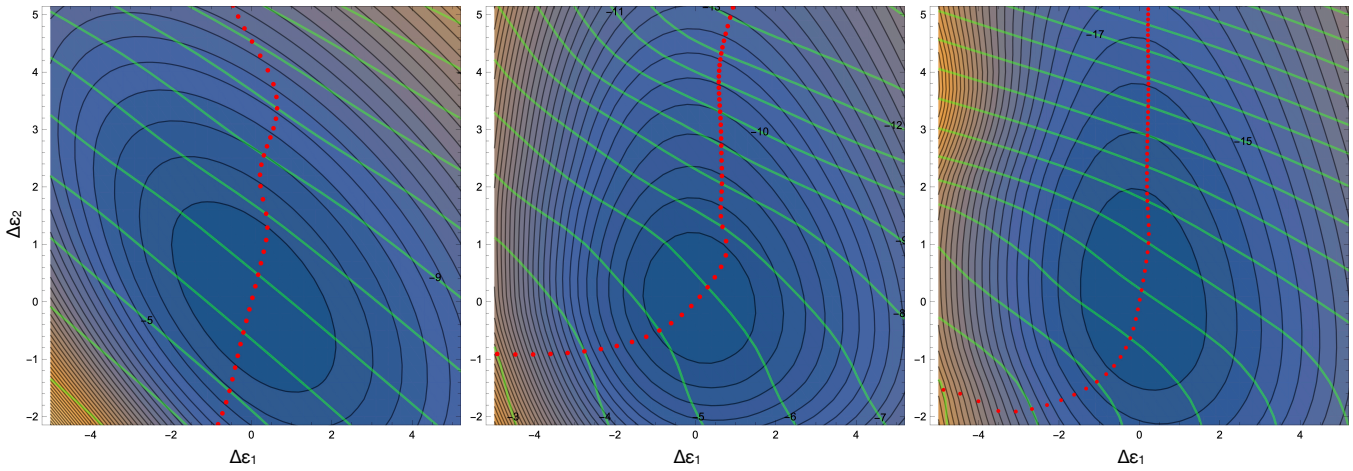


FIG. 9. Contour plot of D_{KL} (shaded contour plot) for the unbinding transition in the 7-particle system as function of $\Delta\epsilon_1, \Delta\epsilon_2$ for a reference path ensemble. Note that the minimum value of D_{KL} is at the origin. On top of the shaded contour plot is a green line contours plot of the predicted rate constant $\ln k_{AB}$, for the settings. Several numerical values of the contours are indicated. The graphical solution to optimisation problem is to pick an imposed green contour and minimize the D_{KL} along this contour. The red points depict this optimal solution. A) fixed cluster, reference path ensemble obtained at $\epsilon_1 = 10, \epsilon_2 = 1.0k_BT$. B) flexible cluster, reference path ensemble. obtained at $\epsilon_1 = 12, \epsilon_2 = 2.0k_BT$. C) flexible cluster, reference path ensemble. obtained at $\epsilon_1 = 15, \epsilon_2 = 5.0k_BT$.

In case of a flexible cluster, as shown in Fig. 9B, the predicted rate constant contours become nonlinear. In Fig. 9C we show a case where the outer and central particles have equal attraction strength.

4. *Optimal parameters for target rate constants*

Next, we would like to find the optimal choice for the force field parameters $\epsilon_{1,2}$. As before, optimising the parameters for a given rate constant amounts to following a green rate constant contour until the D_{KL} is minimal. Using the optimisation procedure outlined in the previous section, we arrive at a prediction given by the red points in Fig. 9. This prediction corresponds thus to the most optimal force field parameters, which minimises the change in the path ensemble with respect to the original force field.

In all cases in Fig. 9, a trivial observation is that the curve passes through the origin, as there the original force field reproduces the original rate constant most optimally. For the fixed cluster Fig. 9A, the optimal curve is roughly vertical, with only a relatively small deviation in ϵ_1. This means that that whether enhancing or reducing the rate, it is always better to change ϵ_2 rather than ϵ_1. Remarkably, this trend even holds for $\Delta\epsilon_2 < -1$, which changes the interaction from attraction to repulsion. This is likely a consequence of the immobility of the particles in this case.

For the flexible cluster cases in Fig. 9B,C, the most striking feature is perhaps the L-shaped curve, indicating a asymmetry concerning reducing the rate or enhancing the rate. For enhancing of the rate, e.g. by one order natural log unit, the red curve shows roughly a linear behavior, that is, $\epsilon_{1,2}$ are contributing to the rate constant in equal proportions. However, when reducing the rate constant further, the curve bends over more vertically, indicating that it is better to change ϵ_2 instead of ϵ_1. In contrast, when increasing the rate, the curve bends over horizontally, indicating that it is now better to change ϵ_1 instead of ϵ_2. This conclusion also holds for Fig. 9C,

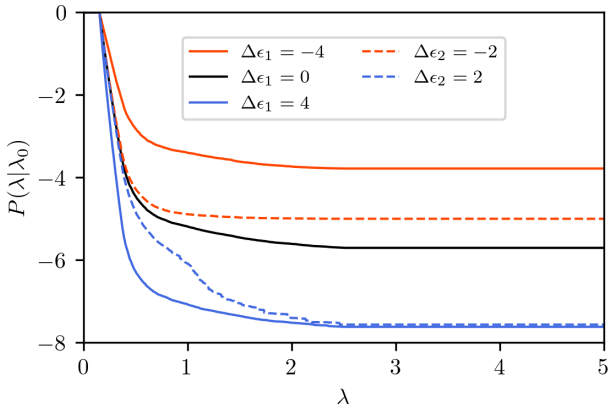


FIG. 10. Reweighted crossing probabilities for the flexible 2D cluster obtained at $\epsilon_1 = 12, \epsilon_2 = 2.0k_BT$. The black solid line is the reference crossing probability. The red and blue curves are reweighed crossing probabilities changing either ϵ_1 (solid) or ϵ_2 (dashed) . Clearly changing ϵ_1 has most effect on the beginning of the crossing probability curves, while changing ϵ_2 in the positive direction has more influence on the latter part, also compared to changing in the negative direction, thus explaining the asymmetry in the binding problem.

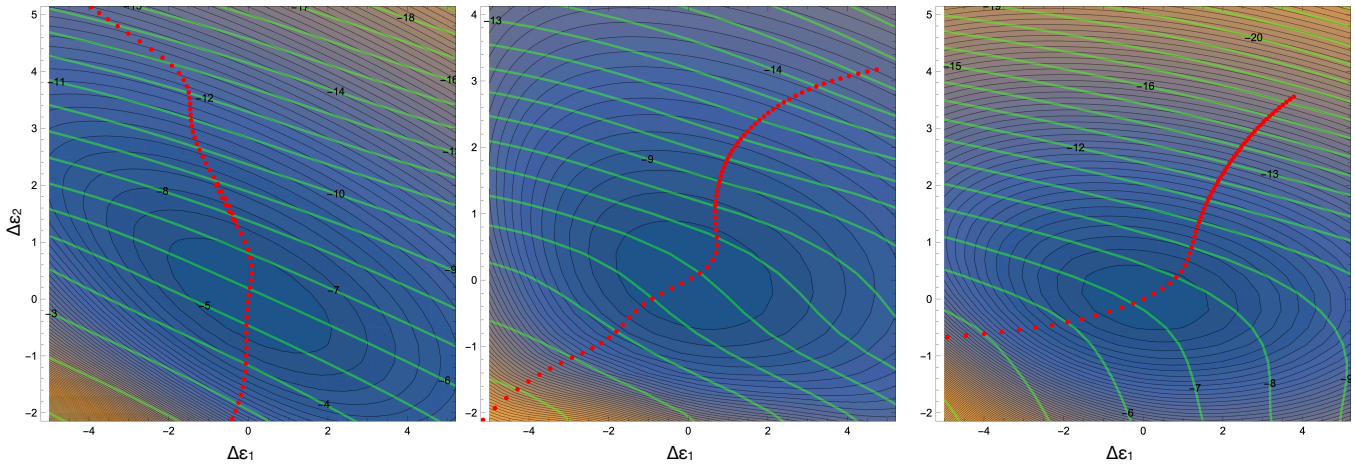


FIG. 11. Contour plot of D_{KL} (shaded contour plot) for the unbinding transition in the 3D 13-particle system as function of $\Delta\epsilon_1, \Delta\epsilon_2$ for a reference path ensemble. Note that the minimum value of D_{KL} is at the origin. On top of the shaded contour plot is a green line contours plot of the predicted rate $\ln k_{AB}$, for the settings. Several numerical values of the contours are indicated. The graphical solution to optimisation problem is to pick an imposed green contour and minimize the D_{KL} along this contour. The red points depict this optimal solution. A) fixed cluster, reference path ensemble. obtained at $\epsilon_1 = 12, \epsilon_2 = 1.0k_BT$. B) flexible cluster, reference path ensemble. obtained at $\epsilon_1 = 12, \epsilon_2 = 2.0k_BT$. C) flexible cluster, reference path ensemble. obtained at $\epsilon_1 = 20, \epsilon_2 = 1.0k_BT$.

where $\epsilon_1 = 15$, and $\epsilon_2 = 5$.

We can interpret this behavior as follows. The best parameters are those that perturb the path ensemble as little as possible. When reducing the rate constant, it is better to adjust the ϵ_2 parameter than the ϵ_1 parameter, even if they both can lead to the same rate constant predictions. This can be interpreted by realising that changing the central particle interaction ϵ_1 will alter the entire reweighted path ensemble: all interface ensembles will be affected. In contrast, change of ϵ_2 will mostly affect only the interface ensembles further out. Since distant interfaces have a (much) lower weight in the ensemble, the perturbation, as measured by the D_{KL} /caliber will be smaller. In contrast, for increasing the rate, changing ϵ_2 will not get you very far, and substantial change of ϵ_1 is also necessary. These effects can be shown by plotting in the total crossing probability for the different settings, in Figure 10. Here it is clear that when looking e.g. at the curves for $\Delta\epsilon_1 = 4$ and $\Delta\epsilon_2 = 2$ the final rate constant predictions (crossing probs) are almost equal, but the intermediate crossing probability, and hence the path ensembles, are very different. Clearly, the $\Delta\epsilon_2 = 2$ case is much closer to the original data set (black solid line), especially in the beginning of the crossing probability where the path ensemble is most dominant.

In Fig. 11 we plot the results for the 3D systems. They are remarkably similar to the 2D systems, showing the robustness of the results. One striking difference is the slope of the green rate constant contours, which is now -0.25 (for the flexible 3D case), as we now have 4 outer particles. So a change in ϵ_2 has a 4-fold effect on the rate constant. Also, the D_{KL} contours appear different, and a bit more skewed compared to the more circular ones in the 2D case. Remarkably, the optimal solution for the parameters (the red curves) look again qualitatively similar to those of the 2D cases. Only for very strong interaction $\Delta\epsilon_2 > 2$ of the outer particles, shown in Fig. 11B,C the red curve bends over.

5. *Comparison with rate constant predictions*

While the prediction of the optimal parameters is already providing valuable insight, the ultimate goal is to establish a better force field model. To assess the quality of the predictions, we can compare the predicted rate constants with a independent calculations at these different force field parameters. Fig. 12 shows this comparison for the flexible 2D unbinding. The agreement is good, especially up to two k_BT from the reference point $(\epsilon_1 = 12, \epsilon_2 = 2.0)$.

6. *Physical insight from the optimization*

These results also reveal several physical aspects: The central particle is more important for increasing the rate, whereas outer particles are more important for decreasing the rate. This is explained by the fact that the entire path ensemble is mostly influenced by the central particle's interaction change, while outer particles only affect the barrier region. Outer particles therefore are prime targets for modulating when reducing the dissociation rate constants. Translating to real proteins this amounts to engineering mutations or post-translational modifications [71] of binding pocket residues close to the surface or modulation of the ligand chemistry in order to

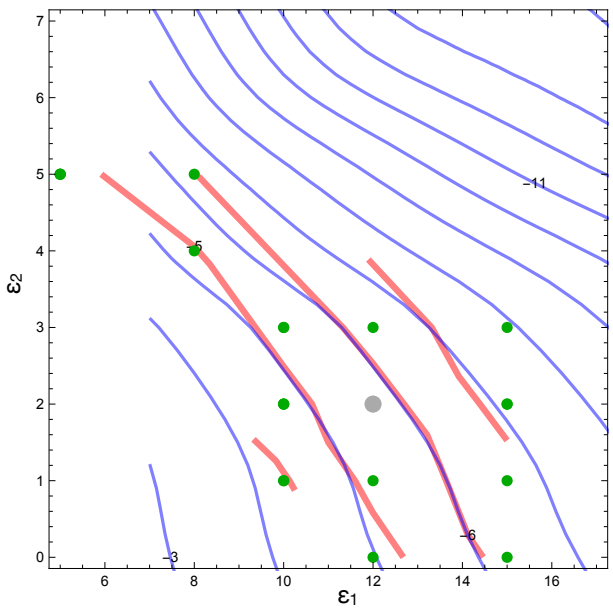


FIG. 12. Contour plot of rate constant predictions (blue) based on the reference ensemble of the flexible 2D cluster obtained at $\epsilon_1 = 12, \epsilon_2 = 2.0 k_B T$ (grey point), compared with red contours interpolated from the true rate constants computed at the indicated green points.

bind better to encounter complex sites at the surface. Of course, this extrapolation to realistic systems is currently no more than a hypothesis, that requires further testing. Yet, the general principle is likely to be robust.

IV. CONCLUSION

In this paper we have introduced a MaxCal based method to optimise force field parameters in order to impose an dynamical constraint, in particular a rate constant in a complex molecular transition. Without any computationally expensive recalculation of the kinetics, the method yields the optimal change in the parameters that leads to an imposed rate constant after the path reweighting, while making the least possible perturbation to the prior trajectory ensemble as measured by the caliber or KL divergence.

We show that the path reweighting leads to meaningful prediction of the rate constants, which agrees with direct calculation for the new force field, even up to more than an order of magnitude suppression of the rate constant in case of the unbinding model. While in this work we develop the methodology and applied it only to simple models, we expect the method to be generally applicable.

Besides a corrected force field, we find that the optimization for multiple parameters allows an interpretation that gives physical insight in which parts of the path ensemble are affected by the parameter changes. Thus, the method provides a powerful tool to inspect rare event trajectory ensembles, and extract valuable information from them. Trajectory ensembles provide us not only with mechanisms, rate constants and transition states for rare event dynamics, but they can also inform on how such properties change with the model parameters. Importantly, they can predict the change in rate constants, and moreover, point us in the direction of parameters that least affect the original path ensembles. This gives the possibility to extend the optimization of force fields that are already optimised for thermodynamics to kinetics. And moreover, gives us pointers to what parts of the systems are most sensitive and thus most sensible to adapt or mutate.

Of course several directions for further research can be considered.

First of all, we have used only the simplest of path actions, i.e. the Onsager-Machlup action for the EM integrator. It is known that EM is not a great integrator, and an obvious extension of the methods would be to extend it to underdamped Langevin integrators [39].

Second, we only have considered up to two parameters. We envision that extension to many parameters is in principle straightforward, but some bookkeeping issues arise, e.g. keeping track of all the cross terms in the square gradient. Nevertheless, the method should be equally effective for optimization in higher dimensions.

Third, the method can and should be applied in a realistic force field, and included in a MD engine. This is non-trivial, since the evaluation of the path action should be done in the integrator. Nevertheless, we believe that this is a worthwhile and necessary research direction, to make our approach useful. One of the issues is the functional form of the potential perturbation. To start, one could try simple functional forms, such as dihedral terms, and Lennard-Jones-like interactions. In a more advanced exploration one could try to use machine learning to learn the functional form of the perturbation.

Fourth, the methods can be pushed beyond the standard atomistic force fields into coarse-grained force fields, for which rate constants are notoriously difficult to reproduce. Such an approach would go beyond a simple adjustment of the diffusion constant, or friction.

Fifth, the method should be also applicable to other dynamical observable, such as diffusion and viscosity. In fact, all observables based on time-correlation functions of a trajectory ensemble should be treatable.

Sixth, parameters beyond the force field might be optimized, including the diffusion, effective mass, and even molecular topology. The holy grail in chemistry, material science and biology is to accurately determine the link between microscopic degrees of freedom such as the chemistry, the microscopic mechanisms, transition rates, structure populations with macroscopic thermodynamic or kinetic properties related to function. Having an efficient algorithm that is able to provide the link between kinetic/thermodynamic macroscopic properties and force field parameters reporting on the underlying physics could be potentially very useful in protein en-

gineering and design of small molecules and of material with tunable macroscopic properties [61–68]. An example of such a design application, are the coarse-grained molecular force fields where sole parameters are the identity of the aminoacid, which are a.o. employed in protein aggregation and protein folding [72, 73]. For such problems one could apply our approach to suggest changes in the aminoacid sequence in the direction of promoting or depressing the rate constant of e.g aggregation, protein folding, or liquid/liquid phase separation. In this way one could optimize the design of novel (bio)material to be further tested in the wet lab, thus bypassing expensive and timely optimization protocols in the wet lab.

Moreover, this method could be particularly useful in chemical reactions, by correcting the kinetics of imperfect while computationally cheap calculations by reactive force fields [74] instead of doing calculations with accurate albeit computationally expensive density functional theory potentials. Another utility is the generality of the method, giving the possibility to combine it with deep learning potentials that are known to be very flexible and have already been used when calibrating force fields for thermodynamics in material science [19, 75].

Finally, our methodology of constrained-optimization based on the Maximum-Entropy is not limited to molecular systems and could even potentially contribute in various problems of time-series, where the underlying dynamics can be modelled as stochastic, undergoing rare events and with a potential energy function reporting on interactions of agents, such as in modeling of stock-market, fluid-flows and health-pandemics. [76–78].

ACKNOWLEDGEMENTS

The authors thank Christoph Dellago and Pieter Rein ten Wolde for useful feedback and helpful discussions.. BGK acknowledges funding by Deutsche Forschungsgemeinschaft (DFG, German Research Foundation) through SFB 1449 – 431232613, sub-project C02. The ideas for this contribution were initiated during the workshop "Accelerating the Understanding of Rare Events" (6-10 September 2021) at the Lorentz Center in Leiden, NL.

Appendix A: Domain of the path integral and path ensemble

1. Fixed path length $\mathcal{T}$

Let $x_i \in \Gamma$ be a point in the configuration or phase space of the molecule. $\mathbf{x}_n = (x_0, x_1 \dots x_n)$ is a time-discretized path of length $\mathcal{T} = n\Delta t$. Ω_n is the space of all paths with this specific length. A domain $\mathcal{S}$ within the path space Ω_n is constructed as a product of subsets of the phase space $S_i \subset \Gamma$, i.e.

$$\mathcal{S}_n = S_0 \times S_1 \cdots \times S_n \,. \tag{A1}$$

where the subset S_i represents the phase space volume in which x_i may be found. The path integral over domain $\mathcal{S}$ then is defined as

$$\int_{\mathcal{S}_n} \mathcal{D}\mathbf{x}_n \, s[\mathbf{x}_n] = \int_{S_0}\int_{S_1}\cdots\int_{S_n} \mathrm{d}x_0\,\mathrm{d}x_1 \dots \mathrm{d}x_n \, s[\mathbf{x}_n] \,, \tag{A2}$$

where $s : \Omega_n \to \mathbb{R}$ is a path space function [37]. The path probability density $\mathcal{P} : \Omega_n \to \mathbb{R}_{\geq 0}$ for paths of fixed length $\mathcal{T}$ is normalized as

$$\int_{\mathcal{S}_n} \mathcal{D}\mathbf{x}_n \, \mathcal{P}[\mathbf{x}_n] = 1 \,, \tag{A3}$$

and a path ensemble average is given as

$$\langle s \rangle_{S_n} = \int_{\mathcal{S}_n} \mathcal{D}\mathbf{x}_n \, \mathcal{P}[\mathbf{x}_n] s[\mathbf{x}_n] \,, \tag{A4}$$

Time-lagged correlation functions $C_{kl}(\mathcal{T})$ between phase space functions $\chi_k : \Gamma \to \mathbb{R}$ and $\chi_l : \Gamma \to \mathbb{R}$, can be written as such a path ensemble average

$$\begin{aligned} C_{kl}(\mathcal{T}) &= \langle \chi_k \chi_l \rangle_{S_n} \\ &= \int_{\mathcal{S}_n = \Omega_n} \mathcal{D}\mathbf{x}_n \, \chi_k(x_0) \mathcal{P}(\mathbf{x}_n) \chi_l(x_n) \end{aligned} \tag{A5}$$

where the path space function only evaluates the initial and the final state of the path $s[\mathbf{x}] = \chi_k(x_0)\chi_l(x_n)$, and the integration is carried out over the entire path space $\mathcal{S}_n = \Omega_n$. This is equation is used when reweighting Markov state models [37–39].

2. Activated paths with fixed path length $\mathcal{T}$

Instead of integrating over all paths with length $\mathcal{T}$, we can restrict the domain of the path integral to activated paths from state $A \subset \Gamma$ to state $B \subset \Gamma$ (and $A \cap B = \emptyset$). An activated path starts in A at time $t = 0$, then leaves A at $t = \Delta t$, samples the transition region $\Gamma \backslash (A \cup B)$ from $t = \Delta t$ until $t = (n-1)\Delta t$, and then enters either A or B. The requirement that the path only enters A or B at the very last step is equal to stating that the path is terminated after it has entered either of the two states. Thus, the domain of the path integral is $A_n = S_0 \times S_1 \cdots \times S_n$ with

$$S_i = \begin{cases} A & i = 0 \\ \Gamma \backslash (A \cup B) & 1 \leq i \leq n-1 \\ A \cup B & i = n \,. \end{cases} \tag{A6}$$

3. Transition path ensemble

When calculating rate constants according to eq. 22, $\int_A \mathcal{D}\mathbf{x}$ denotes a path integral over activated paths of arbitrary length $\mathcal{T}$, i.e.

$$\int_A \mathcal{D}\mathbf{x}\, s[\mathbf{x}] = \sum_{n=3}^{\infty} \int_{A_n} \mathcal{D}\mathbf{x}\, s[\mathbf{x}_n]\,, \tag{A7}$$

where $n = 3$ is the smallest path length that allows an activated path. In eq. A7 we assume that the path function $s[\mathbf{x}_n]$ can suitably be defined for arbitrary path lengths.

The normalization of the path probability for the path integral in eq. A7 is constructed as follows

$$\int_A \mathcal{D}\mathbf{x}\, \mathcal{P}[\mathbf{x}] = \sum_{n=3}^{\infty} \int_{A_n} \mathcal{D}\mathbf{x}\, \mathcal{P}[\mathbf{x}_n] = \sum_{n=3}^{\infty} P_{A,n} = 1\,. \tag{A8}$$

$\int_{A_n} \mathcal{D}\mathbf{x}\, \mathcal{P}[\mathbf{x}_n] = P_{A.n}$ is the probability of an activated path within the ensemble of paths with length $\mathcal{T} = n\Delta t$. Since all paths will eventually enter either A or B, the probability of activated paths decreases with increasing n, and we can assume that the sum converges. In practice, it is sufficient to evaluate the sum up to a maximum path length $n_{\max}$.

An path ensemble average for eq. A7 (as e.g. in eq. 25) is constructed as follows

$$\langle s \rangle_A = \int_A \mathcal{D}\mathbf{x}\, \mathcal{P}[\mathbf{x}] \cdot s[\mathbf{x}] = \sum_{n=3}^{\infty} \int_{A_n} \mathcal{D}\mathbf{x}\, \mathcal{P}[\mathbf{x}_n] \cdot s[\mathbf{x}_n]\,. \tag{A9}$$

In transition path sampling (and transition interface sampling) a transition path ensemble refers to set of activated paths that have been sampled according to eq. A8.

We can reconcile this view with a fixed length L path ensemble, by realising that we can always introduce an additional integral to a path ensemble S_n of the remaining length $L - n$ time slices which normalizes to unity (assuming that all single step probabilities are normalized). Inserting this into the integrals does not change the final outcome.

Appendix B: From eq. 13 to eq. 14

Eq. 13 can be written as

$$D_{KL} = \frac{\mathcal{F}(\mathbf{a})}{\mathcal{Z}(\mathbf{a})} - \ln \mathcal{Z}(\mathbf{a}) + \ln \mathcal{Z}^0 \tag{B1}$$

with $\mathcal{F}(\mathbf{a}) = \mathcal{Z}^0 \int \mathcal{D}\mathbf{x}\, \mathcal{P}^0[\mathbf{x}] e^{w[\mathbf{x},\mathbf{a}]} w[\mathbf{x},\mathbf{a}]$. The derivative of D_{KL} with respect to a parameter a_k then is

$$\frac{\partial}{\partial a_k} D_{KL} = \frac{\mathcal{F}'(\mathbf{a})\mathcal{Z}(\mathbf{a}) + \mathcal{F}(\mathbf{a})\mathcal{Z}'(\mathbf{a})}{\mathcal{Z}^2(\mathbf{a})} - \frac{\mathcal{Z}'(\mathbf{a})}{\mathcal{Z}(\mathbf{a})} \tag{B2}$$

where

$$\mathcal{Z}'(\mathbf{a}) = \frac{\partial}{\partial a_k} \mathcal{Z}(\mathbf{a}) = \mathcal{Z}^0 \int \mathcal{D}\mathbf{x}\, \mathcal{P}^0[\mathbf{x}] e^{w[\mathbf{x},\mathbf{a}]} w'[\mathbf{x},\mathbf{a}] \tag{B3a}$$

$$\begin{aligned} \mathcal{F}'(\mathbf{a}) &= \frac{\partial}{\partial a_k} \mathcal{F}(\mathbf{a}) \\ &= \int \mathcal{D}\mathbf{x}\, \mathcal{P}^0[\mathbf{x}] e^{w[\mathbf{x},\mathbf{a}]} w'[\mathbf{x},\mathbf{a}] w[\mathbf{x},\mathbf{a}] + \\ &\quad \int \mathcal{D}\mathbf{x}\, \mathcal{P}^0[\mathbf{x}] e^{w[\mathbf{x},\mathbf{a}]} w'[\mathbf{x},\mathbf{a}] \\ &= \int \mathcal{D}\mathbf{x}\, \mathcal{P}^0[\mathbf{x}] e^{w[\mathbf{x},\mathbf{a}]} w'[\mathbf{x},\mathbf{a}] w[\mathbf{x},\mathbf{a}] + \mathcal{Z}'(\mathbf{a})\,. \end{aligned} \tag{B3b}$$

Thus,

$$\begin{aligned} \frac{\partial}{\partial a_k} D_{KL} = &\frac{\mathcal{Z}^0 \int \mathcal{D}\mathbf{x}\, \mathcal{P}^0[\mathbf{x}] e^{w[\mathbf{x},\mathbf{a}]} w'[\mathbf{x},\mathbf{a}] w[\mathbf{x},\mathbf{a}]}{\mathcal{Z}(\mathbf{a})} + \\ &\frac{\mathcal{Z}'(\mathbf{a})}{\mathcal{Z}(\mathbf{a})} + \frac{\mathcal{F}(\mathbf{a})\mathcal{Z}'(\mathbf{a})}{\mathcal{Z}^2(\mathbf{a})} - \frac{\mathcal{Z}'(\mathbf{a})}{\mathcal{Z}(\mathbf{a})} \end{aligned} \tag{B4}$$

The two terms $\mathcal{Z}'(\mathbf{a})/\mathcal{Z}(\mathbf{a})$ cancel, and reinserting $\mathcal{F}(\mathbf{a})$, $\mathcal{Z}(\mathbf{a})$, and $\mathcal{Z}'(\mathbf{a})$ yields eq. 14.

[1] A. T. Brünger, P. D. Adams, G. M. Clore, W. L. Delano, P. Gros, R. W. Grossekunstleve, J. S. Jiang, J. Kuszewski, M. Nilges, N. S. Pannu, R. J. Read, L. M. Rice, T. Simonson, and G. L. Warren, Acta Crystallogr. Sect. D Biol. Crystallogr. **54**, 905 (1998).

[2] M. Bonomi, G. T. Heller, C. Camilloni, and M. Vendruscolo, Curr. Opin. Struct. Biol. **42**, 106 (2017).

[3] R. Capelli, G. Tiana, and C. Camilloni, J. Chem. Phys. **148**, 184114 (2018).

[4] Z. F. Brotzakis, M. Vendruscolo, and P. G. Bolhuis, Proceedings of the National Academy of Sciences **118**, e2012423118 (2021).

[5] B. J. Alder and T. E. Wainwright, J. Chem. Phys. **27**, 1208 (1957).

[6] D. Frenkel and B. Smit, *Understanding Molecular Simulation*, 2nd ed. (Academic Press, Inc., Orlando, FL, USA, 2001).

[7] D. E. Shaw, M. M. Deneroff, R. O. Dror, J. S. Kuskin, R. H. Larson, J. K. Salmon, C. Young, B. Batson, K. J. Bowers, J. C. Chao, M. P. Eastwood, J. Gagliardo, and S. C. Gross, Commun. ACM **51**, 91 (2008).

[8] J. E. Stone, J. C. Phillips, P. L. Freddolino, D. J. Hardy, L. G. Trabuco, and K. Schulten, J Comput Chem **28**, 2618 (2007).

[9] G. Ciccotti, C. Dellago, M. Ferrario, E. R. Hernández, and M. E. Tuckerman, European Physical Journal B **95** (2022), 10.1140/epjb/s10051-021-00249-x.

[10] S. A. Hollingsworth and R. O. Dror, Neuron **99**, 1129 (2018).

[11] H. Eyring, J. Chem. Phys. **3**, 107 (1935).

[12] D. Chandler, *Introduction to modern statistical mechanics* (Oxford University Press, 1987).

[13] P. G. Bolhuis and C. Dellago, Rev. Comput. Chem. **27**, 1 (2010).

[14] O. Valsson, P. Tiwary, and M. Parrinello, Annu. Rev. Phys. Chem. **67**, 159 (2016).

[15] J. A. Harrison, J. D. Schall, S. Maskey, P. T. Mikulski, M. T. Knippenberg, and B. H. Morrow, Applied Physics Reviews **5**, 031104 (2018).

[16] S. Piana, K. Lindorff-Larsen, and D. E. Shaw, Biophysical journal **100**, L47 (2011).

[17] D. van der Spoel, Current Opinion in Structural Biology **67**, 18 (2021).

[18] A. Tkatchenko and M. Scheffler, Phys. Rev. Lett. **102**, 6 (2009).

[19] L. Zhang, J. Han, H. Wang, R. Car, and E. Weinan, Phys. Rev. Let. **120**, 143001 (2018), arXiv:1707.09571.

[20] L. Bonati and M. Parrinello, Physical Review Letters **121**, 265701 (2018), arXiv:1809.11088.

[21] A. Singraber, J. Behler, and C. Dellago, J. Chem. Theory Comput. **15**, 1827 (2019).

[22] K. Lindorff-Larsen, P. Maragakis, S. Piana, M. P. Eastwood, R. O. Dror, and D. E. Shaw, PloS one **7**, e32131 (2012).

[23] F. Vitalini, A. S. Mey, F. Noé, and B. G. Keller, The Journal of Chemical Physics **142**, 02B611_1 (2015).

[24] A. Cavalli, C. Camilloni, and M. Vendruscolo, J. Chem. Phys. **138**, 094112 (2013).

[25] W. Boomsma, J. Ferkinghoff-Borg, and K. Lindorff-Larsen, PLoS Comput. Biol. **10**, 1 (2014).

[26] M. Bonomi, C. Camilloni, A. Cavalli, and M. Vendruscolo, Sci. Adv. **2**, 1 (2015).

[27] P. G. Bolhuis, Z. F. Brotzakis, and M. Vendruscolo, The European Physical Journal B **94** (2021), 10.1140/epjb/s10051-021-00154-3.

[28] S.-T. Tsai, E. Fields, and P. Tiwary, , 1 (2022), arXiv:2203.00597.

[29] A. Cesari, S. Bottaro, K. Lindorff-Larsen, P. Banáš, J. Šponer, and G. Bussi, Journal of Chemical Theory and Computation **15**, 3425 (2019).

[30] G. Tesei, T. K. Schulze, R. Crehuet, and K. Lindorff-Larsen, Proceedings of the National Academy of Sciences **118** (2021), 10.1073/pnas.2111696118.

[31] T. Fröhlking, M. Bernetti, N. Calonaci, and G. Bussi, J. Chem. Phys. **152** (2020), 10.1063/5.0011346, arXiv:2004.01630.

[32] A. Varela-Rial, I. Maryanow, M. Majewski, S. Doerr, N. Schapin, J. Jiménez-Luna, and G. De Fabritiis, Journal of Chemical Information and Modeling **62**, 225 (2022).

[33] Y. Qiu, D. G. A. Smith, S. Boothroyd, H. Jang, D. F. Hahn, J. Wagner, C. C. Bannan, T. Gokey, V. T. Lim, C. D. Stern, A. Rizzi, B. Tjanaka, G. Tresadern, X. Lucas, M. R. Shirts, M. K. Gilson, J. D. Chodera, C. I. Bayly, D. L. Mobley, and L.-P. Wang, J. Chem. Theory Comput. **17**, 6262 (2021).

[34] D. C. Rose, J. F. Mair, and J. P. Garrahan, New Journal of Physics **23**, 013013 (2021).

[35] A. Das, D. C. Rose, J. P. Garrahan, and D. T. Limmer, The Journal of Chemical Physics **155**, 134105 (2021).

[36] A. Das, B. Kuznets-Speck, and D. T. Limmer, Phys. Rev. Lett. **128**, 028005 (2022).

[37] L. Donati, C. Hartmann, and B. G. Keller, The Journal of chemical physics **146**, 244112 (2017).

[38] L. Donati and B. G. Keller, The Journal of chemical physics **149**, 072335 (2018).

[39] S. Kieninger and B. G. Keller, The Journal of Chemical Physics **154**, 094102 (2021).

[40] P. G. Bolhuis, D. Chandler, C. Dellago, and P. L. Geissler, Annu. Rev. Phys. Chem. **53**, 291 (2002).

[41] C. Dellago, P. Bolhuis, and P. Geissler, Advances in Chemical Physics **123** (2002).

[42] W.-N. Du and P. G. Bolhuis, The Journal of Chemical Physics **139**, 044105 (2013).

[43] R. J. Allen, P. B. Warren, and P. R. ten Wolde, Physical Review Letters **94** (2005), 10.1103/physrevlett.94.018104.

[44] D. M. Zuckerman and L. T. Chong, Annual Review of Biophysics **46**, 43 (2017).

[45] B. Leimkuhler and C. Matthews, Interdisciplinary applied mathematics **36** (2015).

[46] B. Øksendal, in *Stochastic differential equations* (Springer, 2003) pp. 65–84.

[47] P. E. Kloeden and E. Platen, *Numerical Solution of Stochastic Differential Equations.*, 1st ed. (Springer, Berlin, Heidelberg, 1992).

[48] M. J. Hazoglou, V. Walther, P. D. Dixit, and K. A. Dill, The Journal of Chemical Physics **143**, 051104 (2015).

[49] D. Chandler, J. Chem. Phys. **68**, 2959 (1978).

[50] A. K. Faradjian and R. Elber, Journal of Chemical Physics **120**, 10880 (2004).

[51] R. J. Allen, D. Frenkel, and P. R. Ten Wolde, Journal of Chemical Physics **124** (2006), 10.1063/1.2140273, arXiv:0509499 [cond-mat].

[52] P. Tiwary and M. Parrinello, Physical Review Letters **111**, 230602 (2013).

[53] Z. F. Brotzakis and P. G. Bolhuis, Journal of Chemical Physics **151**, 174111 (2019).

[54] T. van Erp, D. Moroni, and P. Bolhuis, J of chem phys **118**, 7762 (2003).

[55] J. Rogal, W. Lechner, J. Juraszek, B. Ensing, and P. G. Bolhuis, J. Chem. Phys. **133**, 174109 (2010).

[56] C. Dellago and P. G. Bolhuis, Molecular Simulation **30**, 795 (2004).

[57] P. G. Bolhuis and G. Csányi, Physical Review Letters **120**, 1 (2018).

[58] H. Ferrenberg, Alan M.; Swendsen, Robert, Phys. Rev. Lett. **63**, 1195 (1989), arXiv:0302123 [cond-mat].

[59] J. D. Weeks, D. Chandler, and H. C. Andersen, The Journal of Chemical Physics **54**, 5237 (1971).

[60] J. C. Platt and A. H. Barr, NIPS'87: Proceedings of the 1987 International Conference on Neural Information Processing Systems , 612–621 (1987).

[61] R. A. Copeland, D. L. Pompliano, and T. D. Meek, Nat Rev Drug Discov **5**, 730 (2006).

[62] P. J. Tonge, ACS Chemical Neuroscience **9**, 29 (2018).

[63] F. Romano and F. Sciortino, Nature Materials **10**, 171 (2011).

[64] J. S. Oh, S. Lee, S. C. Glotzer, G. R. Yi, and D. J. Pine, Nature Communications **10** (2019), 10.1038/s41467-019-11915-1.

[65] Z. Wang, Z. Wang, J. Li, S. T. H. Cheung, C. Tian, S. H. Kim, G. R. Yi, E. Ducrot, and Y. Wang, Journal of the American Chemical Society **141**, 14853 (2019).
[66] S. Zhang, R. G. Alberstein, J. J. De Yoreo, and F. A. Tezcan, Nature Communications **11**, 1 (2020).
[67] R. S. Fisher and S. Elbaum-Garfinkle, Nature Communications **11** (2020), 10.1038/s41467-020-18224-y.
[68] M. J. Mitchell, M. M. Billingsley, R. M. Haley, M. E. Wechsler, N. A. Peppas, and R. Langer, Nature Reviews Drug Discovery **20**, 101 (2021).
[69] A. Vijaykumar, P. G. Bolhuis, and P. R. ten Wolde, Faraday Discussions **195**, 421 (2016).
[70] A. Vijaykumar, P. R. ten Wolde, and P. G. Bolhuis, The Journal of Chemical Physics **147**, 184108 (2017).
[71] D. L. Winter, H. Iranmanesh, D. S. Clark, and D. J. Glover, ACS Synthetic Biology **9**, 2132 (2020).
[72] G. L. Dignon, W. Zheng, Y. C. Kim, R. B. Best, and J. Mittal, PLoS Computational Biology **14**, 1 (2018).
[73] R. B. Best and G. Hummer, Proceedings of the National Academy of Sciences of the United States of America **113**, 3263 (2016).
[74] T. P. Senftle, S. Hong, M. M. Islam, S. B. Kylasa, Y. Zheng, Y. K. Shin, C. Junkermeier, R. Engel-Herbert, M. J. Janik, H. M. Aktulga, T. Verstraelen, A. Grama, and A. C. Van Duin, npj Computational Materials **2** (2016), 10.1038/npjcompumats.2015.11.
[75] J. Rogal, E. Schneider, and M. E. Tuckerman, Physical Review Letters **123**, 245701 (2019), arXiv:1905.01536.
[76] J.-p. Bouchaud and R. Cont, Eur. Phys. J. B. **6**, 543 (1998), arXiv:9801279 [arXiv:cond-mat].
[77] D. C. Haworth and S. B. Pope, Phys. Fluids **29**, 387 (1986).
[78] L. D. Jones, M. Magdon-Ismail, L. Mersini-Houghton, and S. Meshnick, arXiv:2008.10530 , 1 (2020), arXiv:2008.10530.